Biophysical Journal
Article

Biophysical Society

Electrophysical cardiac remodeling at the molecular level: Insights into ryanodine receptor activation and calcium-induced calcium release from a stochastic explicit-particle model

Sophia P. Hirakis,[1,2] Thomas M. Bartol,[1] Ludovic Autin,[3] Rommie E. Amaro,[2,*] and Terrence J. Sejnowski[1,2,*]
[1]Computational Neurobiology Lab, The Salk Institute of Biological Studies, La Jolla, California; [2]Department of Chemistry and Biochemistry, The University of California San Diego, La Jolla, California; and [3]Department of Integrative Structural and Computational Biology, The Scripps Research Institute, La Jolla, California

ABSTRACT We present the first-ever, fully discrete, stochastic model of triggered cardiac Ca^{2+} dynamics. Using anatomically accurate subcellular cardiac myocyte geometries, we simulate the molecular players involved in Ca^{2+} handling using high-resolution stochastic and explicit-particle methods at the level of an individual cardiac dyadic junction. Integrating data from multiple experimental sources, the model not only replicates the findings of traditional in silico studies and complements in vitro experimental data but also reveals new insights into the molecular mechanisms driving cardiac dysfunction under stress and disease conditions. We improve upon older, nondiscrete models using the same realistic geometry by incorporating molecular mechanisms for spontaneous, as well as triggered calcium-induced calcium release (CICR). Action potentials are used to activate L-type calcium channels (LTCC), triggering CICR through ryanodine receptors (RyRs) on the surface of the sarcoplasmic reticulum. These improvements allow for the specific focus on the couplon: the structure-function relationship between LTCC and RyR. We investigate the electrophysical effects of normal and diseased action potentials on CICR and interrogate the effects of dyadic junction deformation through detubulation and orphaning of RyR. Our work demonstrates the importance of the electrophysical integrity of the calcium release unit on CICR fidelity, giving insights into the molecular basis of heart disease. Finally, we provide a unique, detailed, molecular view of the CICR process using advanced rendering techniques. This easy-to-use model comes complete with tutorials and the necessary software for use and analysis to maximize usability and reproducibility. Our work focuses on quantifying, qualifying, and visualizing the behavior of the molecular species that underlie the function and dysfunction of subcellular cardiomyocyte systems.

SIGNIFICANCE We present the first explicit-particle stochastic model of triggered calcium-induced calcium release in realistic cardiac geometries. Our model features a fully stochastic and physical encounter-based model of Ca^{2+} and ryanodine receptor dynamics and features L-type calcium channels, which dynamically respond to changes in membrane voltage as well as Ca^{2+} concentration. Our model reproduces measurements made both in silico and in vitro. This easily usable and adaptable model is sensitive to alteration of the action-potential waveform and interrogates the subcellular effects of cardiac disease phenotypes, such as geometric alterations.

INTRODUCTION

Topping the list as the world's leading cause of death, heart disease and cardiovascular systems have been a critical research focus for decades (1). In concerted efforts, scientists performing experiments in situ, in vitro, and in silico have examined the collective variables that result in proper cardiac function and, with them, the critical factors that underlie cardiac dysfunction (2). With pieces of information accumulating as a result of experimentation, an important step in our understanding of cardiac systems is the contextualization of scientific findings in working models. By integrating information obtained from multiple spatiotemporal scales and investigation methods, computational models of cardiac systems have provided valuable insights not available to scientists with traditional imaging and experimental

Submitted April 28, 2023, and accepted for publication September 26, 2024.
*Correspondence: ramaro@ucsd.edu or terry@salk.edu
Editor: Jeffrey Saucerman.
https://doi.org/10.1016/j.bpj.2024.09.029

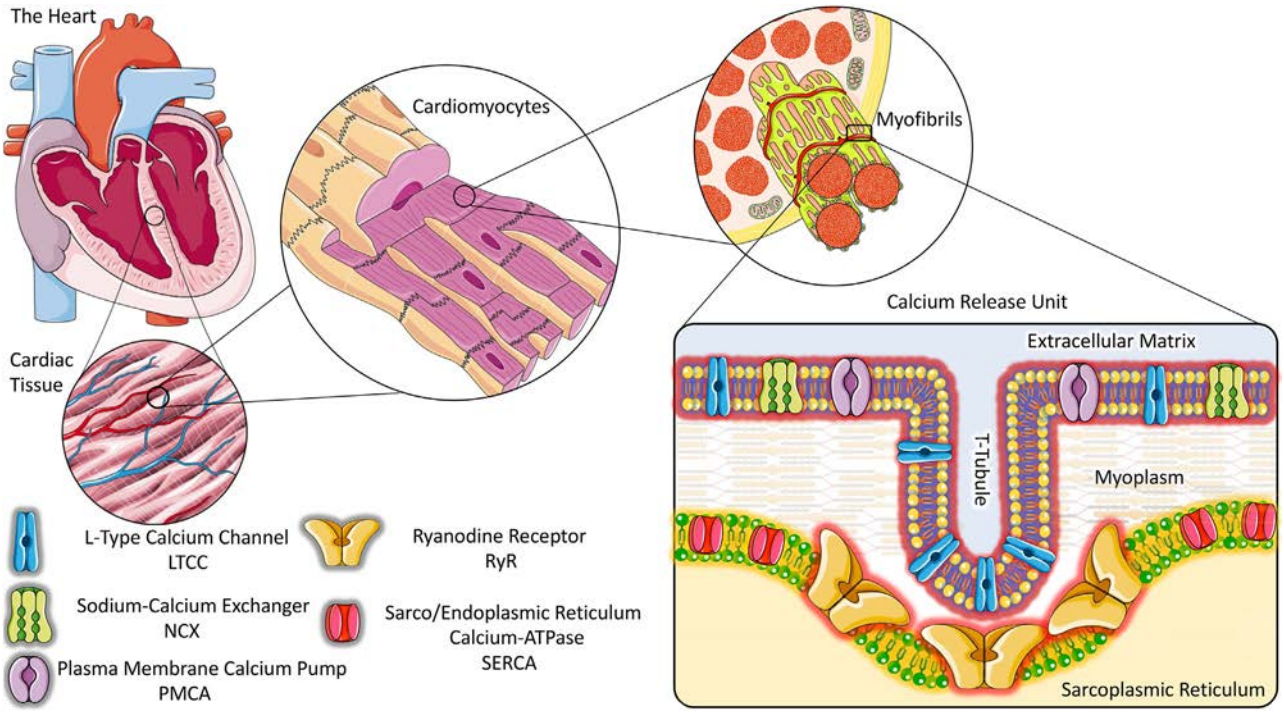

FIGURE 1 Scales of cardiac structure. The structure of the cardiac system can be broken down to the tissue level (cardiac tissue, *middle left*), cellular level (cardiomyocytes, *top middle*), protein level (myofibrils, *top right*), and subcellular level (dyadic junction, *bottom right*). In the dyadic junction, the myocyte membrane, or sarcolemma, forms invaginations called T-tubules (TTs). TTs bring the sarcolemma into close proximity to the sarcoplasmic reticulum (SR) membrane; specifically, LTCCs in the sarcolemma juxtapose RyRs on the SR membrane, creating the dyadic junction. Sodium-calcium exchangers and plasma membrane calcium ATPases (PMCAs) are located on the sarcolemma and sarco/endoplasmic reticulum calcium ATPases (SERCAs) are located on the SR membrane (see the bottom left key for reference). Stock images from smart.servier.com.

methods (3,4). Computational experiments offer users an opportunity to test and validate hypotheses about in situ functions, yielding insights that are inaccessible by other methodologies (5). Due to the breadth of available data at different length and timescales, computationalists are well poised to study cardiac systems in a multiscale fashion (6,7). Fig. 1 shows the various levels of complex structures that make up the cardiac system, demonstrating the multiscale nature of the cardiac structure.

Specialized structures in the sarcolemma or cell membrane were discovered in 1956 (8). Electron microscopy was used to image these invaginations in both axial and transverse directions, later called the transverse-axial tubule system (9). The functional purpose of the transverse tubule (T-tubules, or TTs) is to position the cell membrane directly adjacent to the sarcoplasmic reticulum (SR) membrane to rapidly translate an extracellular signal to an intracellular response. The physical space between the extracellular membrane and the SR membrane is known as the dyadic junction. The narrowness of this dyadic junctional cleft (radius, 10 nm) provides a discrete, restricted space believed to contribute to the sensitivity to small perturbations at the level of Ca^{2+} ions, which underlie cardiac activation mechanisms (10). Within this fundamental region, known as the calcium release unit (CRU), Ca^{2+} dynamics are of utmost importance to the cardiac contraction process, as dysregulation of cellular cardiac Ca^{2+} has been implicated as a source of cardiac dysfunction (2).

Membrane proteins on TTs called L-type calcium channels (LTCCs) (also known as dihydropyridine receptors or voltage-dependent calcium channels) (11) and large proteins (>2 MDa) on the SR membrane proteins called ryanodine receptors (RyRs) (12) were found to be involved in the generation of Ca^{2+} sparks early in the discovery of Ca^{2+} signaling. Although theories about excitation-contraction coupling existed (13), the first Ca^{2+} spark event was visualized only 30 years ago, using laser scanning confocal microscopy (14) and quickly confirmed in subsequent studies (15,16). Within a few years, computer simulations were applied to this system to model the elementary events responsible and to elucidate the subcellular mechanisms visualized with fluorescence measurements (17).

Action potentials (APs) generated in the sinoatrial node of the heart result in the depolarization of the sarcolemma, which leads to the opening of LTCCs in response. Directly adjacent, RyRs sense an increase in cytosolic Ca^{2+} levels as a result of LTCC opening. It is at this point that a signal amplification results, whereby RyRs release thousands of Ca^{2+} ions from the SR into the cell, an event known as

a triggered calcium spark or calcium-induced calcium release (CICR) (18,19). This physical and functional coupling of LTCC and RyR in adjacent TT and SR membranes is known as the couplon (20,21). In response to the increase in cytosolic Ca^{2+}, the inhibition of actin and myosin is relieved by troponin C, which directly binds Ca^{2+}. This causes the muscle fiber proteins to slide across each other, leading to muscle fiber shortening, or muscular contraction, squeezing blood out of the chambers of the heart and out toward the rest of the body. An important SR protein, the sarco/endoplasmic reticulum Ca^{2+}-ATPase (SERCA) pump, clears the high Ca^{2+} levels in the cytosol that result from RyR efflux by refilling SR Ca^{2+} stores, permitting muscle relaxation. This process is repeated every time the heart beats, causing observable changes in cytosolic Ca^{2+} concentration that can be measured and visualized by fluorescence.

Light and electron microscopy are invaluable tools that allow spatial understanding of the intricacies of cellular ultrastructure and function (22,23). Three-dimensional computational modeling of subcellular structures, derived from electron tomography images (24), provided modelers with the first realistic geometries within which simulations could be perfromed just over a decade ago (25). The use of realistic geometries allows for more realistic contextualization of cardiac subcellular models (26), as the cellular structure of cardiomyocytes is extremely complex and organized with details that cannot be accurately encapsulated using idealized structures.

At the scale of single dyadic junctions, even microscopic fluorescence imaging techniques have limitations in terms of their ability to resolve spatial changes in Ca^{2+} levels, especially at short space and timescales. Thus, computational models have played an important role in teasing out the important features of CICR. The field of computational cardiology has an impressive track record of over 30 years of computational modeling of cardiac excitation phenomena that have explained and predicted the mechanisms that underlie Ca^{2+} signaling (2,4,27).

At rest, the average number of Ca^{2+} ions in the CRU is very low. More specifically, the number of Ca^{2+} ions found in the dyadic junction, the region of interest in the CICR process, has been estimated to be statistically less than one (28). At this level, the concepts of continuum concentrations become less meaningful, as the position of Ca^{2+} becomes uncertain. To understand Ca^{2+} dynamics at this level, we require methods that can investigate the probability of collision between molecular species; in this case, ions and protein systems. Moreover, only a fraction of dyadic junctions are known to be activated in synchronous excitation-contraction coupling (29). Most existing models assume a continuous distribution of Ca^{2+} ions, which can oversimplify complex interactions at the cellular level, leading to less accurate predictions of cardiac behavior under stress or disease conditions. Thus, continuum and deterministic modeling methodologies often do not capture the inherent variability and biological complexity that exists in CRU activation systems.

This study aims to specifically address these limitations by 1) implementing a stochastic particle-based approach that more accurately reflects the discrete nature of ion interactions, and 2) applying this model to the direct testing of hypotheses that exist in cardiac stress responses and pathological conditions in heart failure that are thought to contribute to dysregulation in disease morphologies. To more accurately model the dynamics of Ca^{2+} at these fine timescales, we employ a cellular simulation engine called MCell, a stochastic and particle-based approach to modeling reaction-diffusion processes (30–33). The MCell algorithm treats molecular species discretely, tracking the position of each molecule in the system individually. By treating molecules as point particles in space, each molecule can diffuse in three dimensions according to a random walk. Most importantly, reactions between diffusing species occur *only* upon spatial encounter. By treating molecules as individual species rather than part of a continuum, our model reflects the stochastic spatial encounter aspects of biochemical reactions in the cardiac CRU missing in nearly all computational models of CICR.

The first use of stochastic, explicit-particle simulations using MCell to investigate cardiac Ca^{2+} signaling mechanisms was carried out by Koh et al. in 2006 (34). Their study demonstrated how altering dyadic distances affected Ca^{2+} SR fluxes. It featured simplified planar geometries to model the SR and plasma membrane but paved the way for future discrete modeling methods in cardiac systems. Others have used spatial models to investigate the role of molecular players in cardiac Ca^{2+} release (35). In 2012, Hake et al. debuted the first subcellular model of a Ca^{2+} spark (25) using realistic geometries of a cardiac CRU (24). The methods used in the study by Hake et al. were continuum based and deterministic, modeling phenomenological (as opposed to triggered) Ca^{2+} sparks.

In the present study, we describe a model that combines 1) realistic cardiomyocyte geometries with 2) stochastic modeling approaches using particle-based spatial reaction-diffusion approaches to investigate 3) electrophysical cardiac remodeling in heart disease. Our model responds to the need for stochastic and explicit-particle methods to more accurately model the delicate and discrete dynamics of Ca^{2+} at the level of a single CRU (4,28,36). This paper includes a detailed description of our novel stochastic model. We then present a series of experiments designed to validate our model against both computational and florescence experimental data. Finally, the model is used to understand the dysfunction that exists in the morphologies of diseases: the electrophysical and structural remodeling of important membranous proteins and structures critical for the proper function of the cardiac system, concluding with

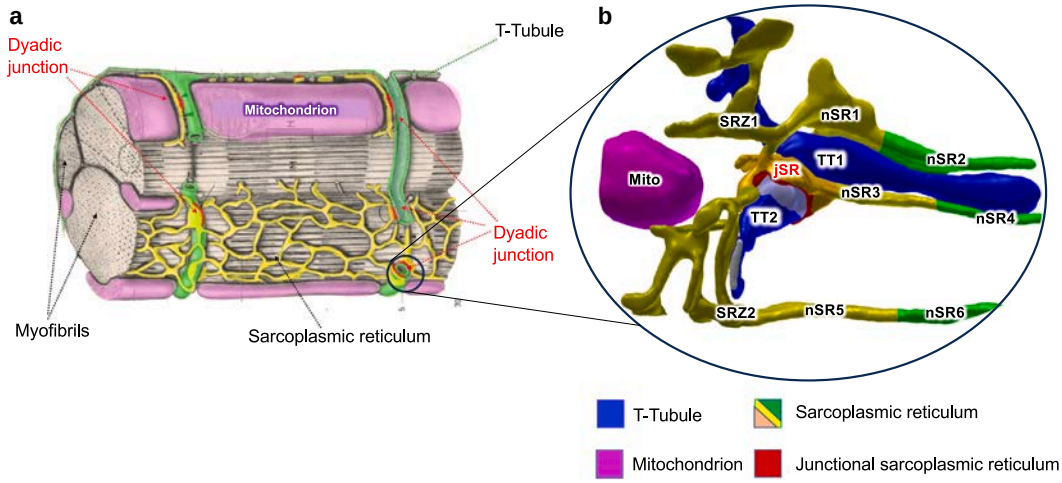

FIGURE 2 The CRU. (*a*) The cellular ultrastructure of the myocardium. The myofibrils (*gray*) longitudinally line the muscle cells and the mitochondria (*purple*) are dispersed throughout. The sarcolemma (plasma membrane) (*green*) creates axial invaginations called transverse tubules (T-tubules or TT, green) that come into close contact with the web of the SR (*yellow*) in a region known as the dyadic junction (*red*). (Image provided and colored by Masahiko Hosijima, from the Textbook of Histology (1969) by W. Bloom and D.W. Fawcett.) (*b*) The calcium release unit (CRU) geometry used in our simulations. The SR (*green*, *yellow*, *orange*) is subdivided into network SR (nSR1, nSR2, nSR3, nSR4, nSR5, nSR6) Z-line SR (SRZ1, SRZ2), and junctional SR (jSR; *red*). The axial T-tubule (TT1) and the transverse T-tubule (TT2) (*blue*) are proximal to the SR. A single mitochondrion (Mito; *magenta*) is shown in the geometry for two-dimensional clarity, although two mitochondria exist in the geometry.

a discussion of the implications of the model for future research and clinical practice.

MATERIALS AND METHODS

Building the geometric model

The realistic geometry of the mouse myocardium used in this model is the result of transmission electron microscopy (TEM) images taken by Hayashi et al. (24), segmented with IMOD (37). The geometry (see Fig. 2 *b*) features a contiguous SR, one axial and one transverse tubule (TT1 and TT2, respectively), and two mitochondria (Mito1 and Mito2). To be usable by our simulation interface and engine (CellBlender and MCell, respectively), it was necessary to further refine the mesh. For this, we used an improved version of GAMer developed at the National Biomedical Computational Resource (NBCR) at the University of California, San Diego (UCSD) (38,39).

The original mesh files were provided to us by Dr. Johan E. Hake. To divide the mesh into objects usable by MCell and CellBlender, we used the color information attributed to the data as a way to classify separate model objects. The model objects are named as follows: 1) T-tubule 1 (TT1, axial); 2) T-tubule 2 (TT2, transverse); 3) mitochondrion 1 (Mito1); 4) mitochondrion 2 (Mito2); 5) SR. The SR was further subdivided into surface regions used in our model: network SR (nSR), Z-line SR (SRZ), and junctional SR (jSR) subdivided in the following ways: a) nSR1, nSR2, nSR3, nSR4, nSR5, nSR6; b) SRZ1, SRZ2; c) jSR release site, jSR rim, jSR back, preserving the original nomenclature used by Hake et al. (25). Specific volume information for these structures can be found in the supporting material (Table S5).

In addition, we were provided the original TEM images by Dr. Masahiko Hoshijima from the National Computational Microscopy Imaging Resource. The tomograms included roughly segmented RyR locations in our specific junctional SR region (40). Although the exact positions and orientations of RyRs were not clearly discernible, we counted a total of 96 receptors in the junction. We augmented the unresolved RyR positions in our CRU geometry by incorporating center-to-center distance data (41) provided by Dr. Parisa Asghari. Finally, open-state cryoelectron microscopy images of RyR2 (PDB: 5GOA (42)) were used to space-fill the junctional SR membrane, ensuring that the center of RyR2 could fit accurately within the final positions chosen in the geometry.

The MCell model of the CRU

Using MCell, the exact positions and numbers of the molecules that comprise our system are tracked and counted. The molecules are modeled as point particles that diffuse according to specified molecular diffusion rates according to the equations of Brownian motion (30). Reactions can be unimolecular (state transitions) or bimolecular, occurring only upon spatial encounter. Bimolecular reactions can occur between two cytosolically diffusing molecules (volume molecules), a volume molecule and a membrane-bound species (surface molecule), or between two surface molecules. The Monte Carlo algorithm used by MCell employs a pseudo-random number generator that ensures each simulation trial, with a different seed to initialize the pseudo-random number generator, will give an independent result.

Our CRU MCell model features cytosolic and SR Ca^{2+} buffers that are routinely used by other modelers: in the cytosol, ATP (25,43,44), calmodulin (CMDN) (44–47), troponin C (48), and Fluo-4 (44); and in the SR, calsequestrin (CSQN) (43,44,49) and Fluo-5 (44). Several adaptations were necessary to create a truly discrete and elementary model that tracked individual Ca^{2+} species. These were mainly related to the proteins responsible for the translocation of Ca^{2+} across membranes. As most available models do not count individual Ca^{2+}, we adapt analogous and well-suited descriptions of the behavior of the following protein systems: plasma membrane calcium-ATPase (PMCA) (5,50,51), sodium-calcium exchanger (NCX) (5,52), SERCA pump (5,53), and RyR (54). The most critical feature of these systems is their ability capture the kinetic behavior of individual proteins interacting with a single Ca^{2+} species. Considerable adaptation and calculations were necessary to achieve steady-state homeostatic behavior in the absence of stimulus, which is detailed in the corresponding molecule description sections, as well as in the supporting material.

Studies by Hake et al. (25) focused their efforts on studying Ca^{2+} spark termination, using a phenomenological model of RyR that occupies one of two states: on or off. As such, RyR activity was preset, and not activated in

TABLE 1 Parameters of Calcium Buffering Species

Parameter	Description	Value	Units	Reference
$D^{cyt}Ca$	diffusion constant of Ca^{2+}(in cytosol and SR)	2.2×10^{6}	$cm^{2}\ s^{-1}$	Hake et al. (2012); Louch et al. (2010)
$[Ca^{2+}]_{cyt}$	initial concentration of Ca^{2+} in cytosol	140×10^{-9}	M	Hake et al. (2012)
$[ATP - Ca]_{cyt}$	Ca^{2+}-bound ATP concentration in cytosol	318×10^{-9}	M	Hake et al. (2012)
${}^{ATP}k_{on}$	ATP Ca^{2+} on rate constant	2.25×10^{8}	$M^{-1}\ s^{-1}$	Hake et al. (2012); Picht et al. (2011); Bers (2001)
${}^{ATP}k_{off}$	ATP Ca^{2+} off rate constant	450×10^{2}	s^{-1}	Hake et al. (2012); Picht et al. (2011)
$D^{cyt}CMDN$	diffusion constant of CMDN in cytosol	25×10^{-8}	$cm^{2}\ s$	Hake et al. (2012); Michailova et al. (2002)
$D^{cyt}CMDN\_Ca$	diffusion constant of Ca^{2+}-bound CMDN in cytosol	x 10^{-6}	$cm^{2}\ s^{-1}$	Hake et al. (2012);
$[CMDN]_{cyt}$	free CMDN concentration in cytosol	23.529×10^{-6}	M	Hake et al. (2012); Fabiato (1983)
$[CMDN - Ca]_{cyt}$	Ca^{2+}-bound CMDN concentration in cytosol	471×10^{-9}	M	Hake et al. (2012)
${}^{CMDN}k_{on}$	CMDN Ca^{2+} on rate constant	34×10^{6}	$M^{-1}\ s^{-1}$	Hake et al. (2012); Robertson et al. (1981); Picht et al. (2011)
${}^{CMDN}k_{off}$	CMDN Ca^{2+} off rate constant	238	s^{-1}	Hake et al. (2012); Robertson et al. (1981)
$D^{cyt}TRPN$	diffusion constant of troponin C in cytosol	0	$cm^{2}\ s^{-1}$	Hake et al. (2012)
$D^{cyt}TRPN\_Ca$	diffusion constant of Ca^{2+}-bound troponin C in cytosol	0	$cm^{2}\ s^{-1}$	Hake et al. (2012)
$[TRPN]_{cyt}$	free troponin C concentration in cytosol	56.8×10^{-6}	M	Hake et al. (2012); Bondarenko et al. (2004)
$[TRPN - Ca]_{cyt}$	Ca^{2+}-bound troponin C concentration in cytosol	13.2×10^{-6}	M	Hake et al. (2012)
${}^{TRPN}k_{on}$	troponin C Ca^{2+} on rate constant	32.7×10^{6}	$M^{-1}\ s^{-1}$	Hake et al. (2012); Bondarenko et al. (2004)
${}^{TRPN}k_{off}$	troponin C Ca^{2+} off rate constant	19.6	s^{-1}	Hake et al. (2012); Bondarenko et al. (2004)
$D^{cyt}Fluo4$	diffusion constant of Fluo-4 in cytosol	42×10^{-8}	$cm^{2}\ s^{-1}$	Hake et al. (2012); Picht et al. (2011)
$D^{cyt}Fluo4\_Ca$	diffusion constant of Ca^{2+}-bound Fluo-4 in cytosol	42×10^{-8}	$cm^{2}\ s^{-1}$	Hake et al. (2012)
$[Fluo4]_{cyt}$	free Fluo-4 concentration in cytosol	22.186×10^{-6}	M	Hake et al. (2012); Picht et al. (2011)
$[Fluo4 - Ca]_{cyt}$	Ca^{2+}-bound Fluo-4 concentration in cytosol	2.82×10^{-6}	M	Hake et al. (2012)
${}^{Fluo4}k_{on}$	Fluo-4 Ca^{2+} on rate constant	110×10^{6}	$M^{-1}\ s^{-1}$	Hake et al. (2012); Picht et al. (2011)
${}^{Fluo4}k_{off}$	Fluo-4 Ca^{2+} off rate constant	110	s^{-1}	Hake et al. (2012); Picht et al. (2011)
$[Ca^{2+}]_{sr}$	initial concentration of Ca^{2+} in SR	1.3×10^{-3}	M	Hake et al. (2012)
$D^{sr}Fluo5$	diffusion constant of Fluo-5 in SR	8×10^{-8}	$cm^{2}\ s^{-1}$	Hake et al. (2012); Picht et al. (2011)
$D^{sr}Fluo5\_sr$	diffusion constant of Ca^{2+}-bound Fluo-5 in SR	8×10^{-8}	$cm^{2}\ s^{-1}$	Hake et al. (2012)
$[Fluo5]_{sr}$	free Fluo-5 concentration in SR	5.9×10^{-6}	M	Hake et al. (2012); Picht et al. (2011)
$[Fluo5 - Ca]_{sr}$	Ca^{2+}-bound Fluo-5 concentration in SR	19.1×10^{-6}	M	Hake et al. (2012)
${}^{Fluo5}k_{on}$	Fluo-5 Ca^{2+} on rate constant	110×10^{6}	$M^{-1}\ s^{-1}$	Hake et al. (2012); Picht et al. (2011)
${}^{Fluo5}k_{off}$	Fluo-5 Ca^{2+} off rate constant	110	s^{-1}	Hake et al. (2012)
$D^{sr}CSQN$	diffusion constant of CSQN in SR	0	$cm^{2}\ s^{-1}$	Hake et al. (2012)
$D^{sr}CSQN\_Ca$	diffusion constant of Ca^{2+}-bound CSQN in SR	0	$cm^{2}\ s^{-1}$	Hake et al. (2012)
$[CSQN]_{sr}$	free CSQN concentration in SR	56.8×10^{-6}	M	Hake et al. (2012); Bondarenko et al. (2004)
$[CSQN - Ca]_{sr}$	Ca^{2+}-bound CSQN concentration in SR	13.2×10^{-6}	M	Hake et al. (2012)
${}^{CSQN}k_{on}$	CSQN Ca^{2+} on rate constant	32.7×10^{6}	$M^{-1}\ s^{-1}$	Hake et al. (2012); Bondarenko et al. (2004)
${}^{CSQN}k_{off}$	CSQN Ca^{2+} off rate constant	19.6	s^{-1}	Hake et al. (2012); Bondarenko et al. (2004)
NH_{max}	CaC SR refill rate	15.7×10^{5}	s^{-1}	derived
k_{max}	CaC SR absorption rate	11.7×10^{8}	$M^{-1}\ s^{-1}$	derived

response to any form of an extracellular, electrical signal. The number of open receptors was set to a constant number (five) and the efflux of Ca^{2+} through RyRs was terminated in response to a SR Ca^{2+} concentration that was preset by the model builders with a hard-coded termination time (28.5 ms). To cross-validate our stochastic and particle-based methods with already-established deterministic, continuum methods, we created a "dual-state RyR model" to mirror the aforementioned phenomenological RyR behavior. Considerable testing, described in the supporting material and results sections, was done to ensure that our experiments matched observables derived from both computational and bench experiments. Upon successfully matching our base-line model output to experimental observables, we sought to model triggered Ca^{2+} sparks.

Couplon dynamics are the fundamental processes underlying CICR. Electrical stimulation drives the dynamic interplay between LTCC and RyR. To model this phenomenon explicitly, spatially, and stochastically, we incorporated a model of LTCC that responds to sarcolemmal excitation. Greenstein and Winslow previously described both voltage-dependent and calcium-dependent activation and inactivation properties (55) of LTCC and this model has been tested extensively. With this AP-driven LTCC model, RyRs can respond dynamically to Ca^{2+} sparklets generated by LTCC openings in response to voltage changes across the T-tubule membrane.

Most importantly, in this current modeling regime, Ca^{2+} sparks are generated *only* upon the spatial encounter of individual Ca^{2+} ions with individual RyRs in the dyadic junction. In the following subsections, we describe the dynamics of Ca^{2+} in 1) the cytosol and within SR by Ca^{2+} buffers; 2) across the T-tubule membrane (extracellular Ca^{2+} fluxes) with PMCA, NCX, and LTCC; and 3) throughout the SR network (intracellular Ca^{2+} fluxes) with SERCA2a and RyR2. The parameters used to describe the molecular diffusion and kinetic states are listed in Table 1, as well as Tables S1–S4 in the supporting material. We report a performance of 0.2 wall-clock hours per 300-ms simulation on a single-core 3-GHz Intel Xeon processor.

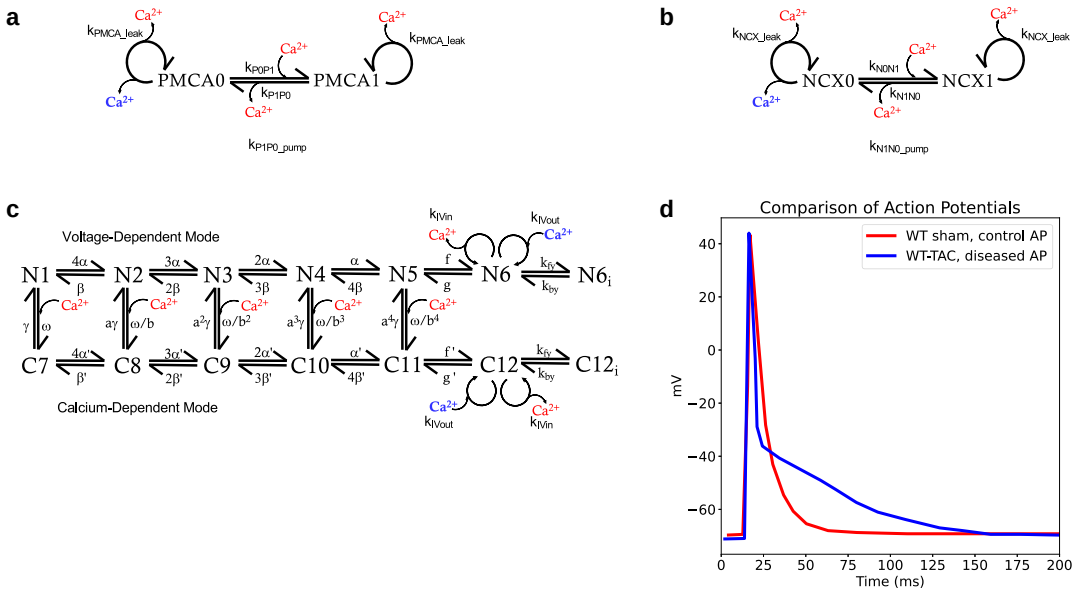

FIGURE 3 Sarcolemmal (T-tubule) fluxes. (*a*) PMCA model. Adapted from the model by Bartol et al. (2015) and based on measurements by Brini and Carafoli (2009) and Penheiter et al.(2003). (*b*) Sodium/calcium exchanger model. Adapted from the model by Bartol et al. (2015) and based on measurements by Hilgemann (1991). (*a* and *b*) Both states are capable of leaking Ca^{2+} into the cytoplasm (*red*), corresponding to a background Ca^{2+} concentration of 140 mM. The transition from states 0 to 1 pump one Ca^{2+} ion per reaction into the extracellular space (*blue*). Reaction rate constants can be found in Table S1. (*c*) LTCC model adapted from the model by Greenstein and Winslow (2002). The model features voltage-dependent and calcium-dependent modes and is capable of pumping Ca^{2+} into (*red*) and out (*blue*) of the T-tubule space. (*d*) LTCC APs. Control AP, WT-sham (*red*), and disease AP, TAC, WT-TAC (*blue*) APs used to stimulate LTCC, based on the model by Wang et al. (2013).

Biochemical system design

Endogenous and exogenous calcium buffering

The kinetics of the cytosolic and SR Ca^{2+} buffers are modeled according to Eq. 1. The buffer mechanism is a simple two-step reaction, where the buffer can exist in apo (B) or Ca^{2+}-bound states ($B \cdot Ca^{2+}$). All buffer molecules diffuse in three dimensions throughout the system with the exception of TRPN and CSQN. The parameters of molecular diffusion and reaction kinetics are found in Table 1. Rate derivations for the forward and reverse reactions, as well as equilibrium concentrations can be found in the supporting material (see Eqs. S1, S2, S3, S4, S5, S6, and S7).

$$B + Ca^2 + \underset{k_r}{\overset{k_f}{\rightleftharpoons}} \underset{\text{Calcium}-\text{bound buffer}}{B \cdot Ca^{2+}} \tag{1}$$

T-tubule membrane fluxes

PMCA and NCX fluxes

There are two main sarcolemmal pumps known to maintain homeostasis in cardiomyocytes: the PMCA pump and the NCX pump (28). Typically, sarcolemmal pumps are modeled with three separate fluxes: PMCA (also known as pCa), NCX, and a background Ca^{2+} flux (also called Cab). We model our PMCA and NCX pumps as dual-state reactions in which an ion of Ca^{2+} can reversibly bind to the first state, and, in a separate irreversible reaction, Ca^{2+} is pumped out of the cytosol (see Fig. 3 *a* and *b*; Eq. 2). The background Ca^{2+} flux is captured with "leak" reactions in both our PMCA and NCX models. The kinetic rates used in the model for both PMCA and NCX can be found in Table S1 in the supporting material. In the interest of brevity, mathematical derivations of the rates can be found in the supporting material, corresponding to Eqs. S8–S16.

$$PMCA0 + Ca^2 + \underset{k_{-1}}{\overset{k_1}{\rightleftharpoons}} \underset{\text{Calcium}-\text{bound pump}}{PMCA1} \overset{\text{pump}}{\rightarrow} PMCA0 \tag{2}$$

L-type calcium channel flux

Modeling CICR necessitated an AP-mediated excitation mechanism of LTCC Ca^{2+} influx to trigger Ca^{2+} efflux from the SR through RyR. To model voltage-gated, AP-driven, or triggered CICR, we adapted the well-established model of LTCC dynamics developed by Greenstein and Winslow (55) to be used in our explicit-particle system. This LTCC model features both voltage-dependent modes and calcium-dependent modes. In this way, we were able to model the rate constants of LTCC state transitions as a function of membrane Ca^{2+} reactions, voltage, and time (see Fig. 3 *c*). The LTCC is mathematically described in the supporting material.

To demonstrate the sensitivity of our implemented LTCC model to changes in AP shape, we added the option for the user to change AP inputs using a parameter called, "ap_mode". Outside of validation experiments, LTCC are stimulated using wild-type (WT)-sham APs as a control, and trans-aortic constriction (TAC) APs, as modeled by Wang et al. (56) (see Fig. 3 *d*), to reflect a diseased state.

AP

The LTCC is activated in response to the depolarization of the T-tubule membrane experienced as a result of an AP. It is known that, in diseased cardiac systems, the shape of the AP is affected (57). To model the effects of the AP shape on our system, MCell uses variable reaction rates attributed to the different LTCC reactions. Experiments by Wang et al. produced the two APs used in this model: 1) control AP, a WT sham AP; and 2) disease AP, a trans-aortic constriction model (56). The shape of the AP was digitized by an internal script named FigureData.py. The xmgrace program was used to perform an Akima-spline interpolation to increase the time resolution of the AP for MCell to accurately adjust to changes in membrane

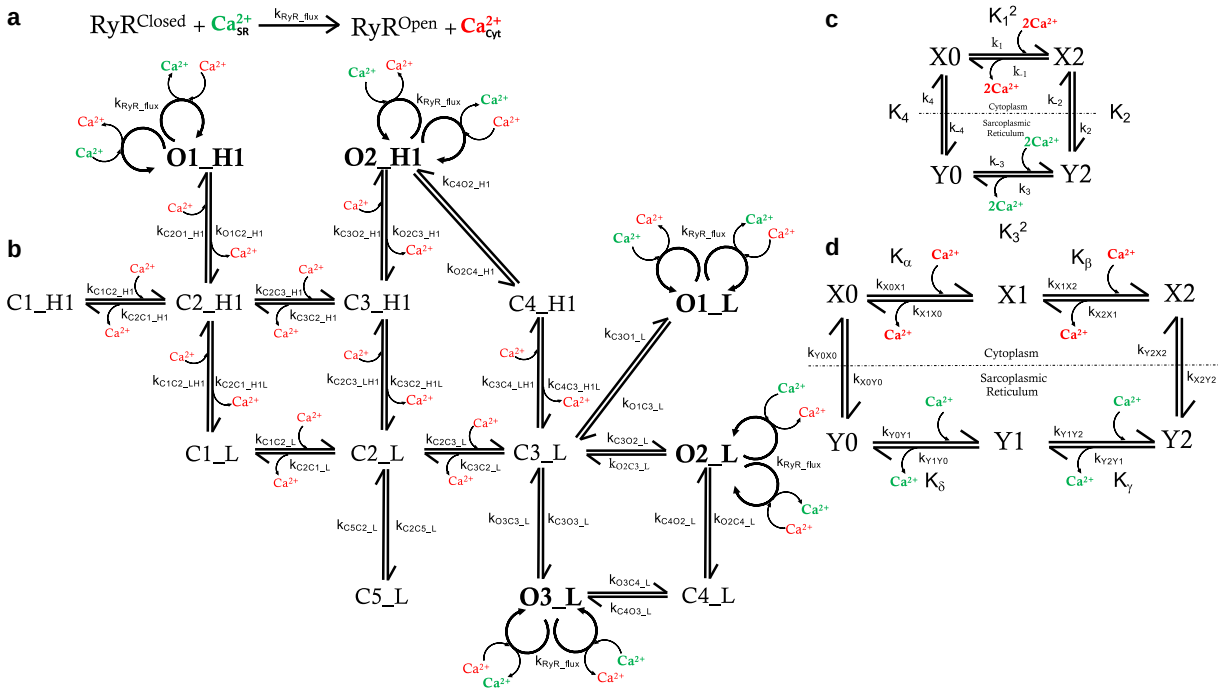

FIGURE 4 SR flux models. (*a*) Dual-state model of RyR, developed in MCell to recreate experimental observables made by Hake et al. (2012). SR Ca^{2+} (*green*) binds to RyR in the closed state, and, when the channel is open, cytosolic Ca^{2+} (*red*) is released until the preset termination time is reached. The rate is variable, and the channel opens and closes based on the "on" or "off" state. (*b*) Multi-state model of RyR2. Adapted from the Markov Model by Saftenku et al. (2001). Nine closed (C) states and five open (O) states describe the kinetic scheme of the RyR. Cytosolic Ca^{2+} (*red*) binds to closed states in high (H1) and low (L) gating modes. In open states, SR Ca^{2+} (*green*) and cytosolic Ca^{2+} are translocated through the receptors. The reaction rates can be found in Table S4 (*c*) Original four-state SERCA model developed by Higgins et al. (2006). Two Ca^{2+} ions are absorbed and released in a single step, and thus this coarse-grained model is not suitable for modeling Ca^{2+} discretely. (*d*) Six-state SERCA model adapted from Higgins et al. (2006). Three cytoplasmic-facing states (X) and three sarcoplasmic reticulum-facing states (Y) discretely translocate cytosolic Ca^{2+} (red) to Ca^{2+} of the SR (*green*). The reaction rate constants can be found in Table S3 and the derivation of the reaction rates is described in the Eqs. S34–S60.

voltage on the T-tubule. Time is then converted into seconds for use in the model. The gen_LTCC_Greenstein_Winslow_rates.py script converts the raw data from the AP to variable rates that can be used by the MCell engine. The resulting variable rates and the scripts used to generate them are included in the supplementary files.

SR fluxes

Modeling a continuous SR calcium network

Because this model represents only a single dyadic junction, it is necessary to model the boundary conditions at the truncated ends of our small sample of SR network in a way that makes it behave as if it were contiguous with a complete SR. For instance, refill times as a result of Ca^{2+} spark activity presented a challenge, as SERCA pumps are generally localized outside of the dyadic junction (58). The fine nature of our mesh—specifically the area of the effector tile (A_{ET})—as well as the high Ca^{2+} concentration in the SR lead to the implementation of a "throttled flux" boundary condition, a technique quite different from the traditional "concentration clamp" feature available in MCell. To do this, we use a molecular species, the calcium creator (CaC) that accurately maintains the Ca^{2+} concentration in the SR according to experiments by Picht et al. (see Fig. 5 *a*) and that recovers from Ca^{2+} transients with a user-defined time constant. The reaction for CaC refill and absorption is described by Eq. 3. The derivation of the parameters used to develop the CaC model is described in the supplement (Eqs. S27–S33). CaC is placed on the capping regions of our network mesh, where the SR ends and is truncated from the rest of the continuous system. In total, four CaC molecules are placed, one at each end of the network SR mesh (nSR2, nSR6) and two in the arms of SRZ2. This simple, yet computationally efficient method addresses the boundary condition problem and maintains a level of Ca^{2+} in the SR network, ensuring continuity with a subcellular environment that is not explicitly modeled.

$$\mathrm{CaC} \underset{\mathrm{SR_{absorption}}}{\overset{\mathrm{SR_{refill}}}{\rightleftharpoons}} \mathrm{CaC} + \mathrm{Ca}^{2+} \tag{3}$$

SERCA pump kinetics

Of utmost importance in the dynamics of Ca^{2+} during the phenomenon of CICR is the action of the cardiac SERCA2a pump, which is responsible for the refilling of the SR, clearing of an estimated 70%–90% of cardiomyocyte Ca^{2+} after a release event (28). Most importantly, SERCA maintains homeostatic equilibrium in cardiac myocytes by clearing Ca^{2+} brought into the cell by PMCA, NCX, LTCC, and RyR. In a single forward cycle of the SERCA pump, one molecule of ATP is consumed to translocate two ions of Ca^{2+} from the cytoplasm to the SR, the intracellular Ca^{2+} store (see Fig. 4 *c*). To explicitly model the dynamics of Ca^{2+} in the myoplasm and inside the SR required discrete models that treated Ca^{2+} binding, pumping, and release as individual reactions. To achieve this, we adapted a SERCA model (Fig. 4 *d*) originally developed by Higgins et al. to bind Ca^{2+} ions individually (53). This model has been used in previous work to reproduce the dynamics of SERCA2a in maintaining a 140-nM cytoplasmic Ca^{2+} concentration while satisfying microscopic reversibility at a temperature of $37^{\circ}C$ (5).

The original four-state, nonelementary kinetic model of Higgins et al. (Fig. 4 *c*) was expanded to a six-state elementary kinetic model with

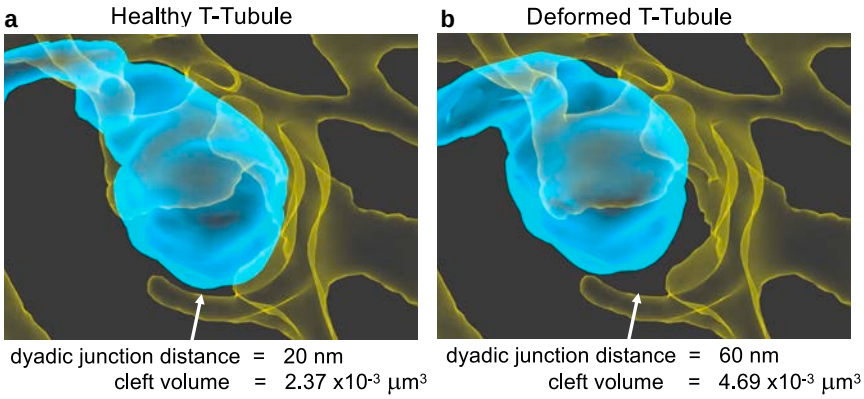

FIGURE 5 Comparison of WT and deformed T-tubule dyadic junction volumes. (*a*) The WT T-tubule (*blue*) forms a dyadic junction of volume $2.37 \times 10^{-3} \mu m^3$ against the SR (*yellow*). (*b*) The deformed T-tubule (*blue*) forms a dyadic junction of volume $4.69 \times 10^{-3} \mu m^3$ against the SR (*yellow*). The deformed dyadic junction volume is roughly twice that of the WT dyadic junction volume.

cytoplasmic (X) and SR (Y) interaction states to capture individual binding of two Ca^{2+} ions, discretely (Fig. 4 *d*). Cytosolic Ca^{2+}-binding states are designated as X and SR Ca^{2+}-binding states are designated as Y. The numbers assigned to the states reflect the number of Ca^{2+} that are bound to the state. For example, X0 has zero Ca^{2+} bound; X1 has one Ca^{2+} bound; X2 has two Ca^{2+} bound.

We assume a concentration of 1.3 mM Ca^{2+} in the lumen of the SR, as modeled by others (25). The value of k_{on} between X1 and X2 and between Y1 and Y2 was set to $1 \times 10^8 M^{-1} s^{-1}$ to maintain microscopic reversibility. The values of K_D specified by Higgins et al. were used to calculate k_{off}. As in Higgins et al., the model was constrained to satisfy the Gibbs free energy of ATP binding and hydrolysis. The surface grid density of SERCA2a on the SR was set to 13,000µm^{-2}. This is the maximum allowed SERCA density on our mesh, despite estimates of SERCA on nonjunctional SR membrane being 31,000–34,000 µm^{-2} according previous studies (59). The mathematical derivations of the rates expanding the four-state, implicit Ca^{2+}-binding model to an explicit six-state model are described in the supporting material (Eqs. S34–S60), and the kinetic variables can be found in Table S3.

RyR kinetics

A model of triggered Ca^{2+} sparks would not be complete without the major SR Ca^{2+}-release channel, RyR. For the purpose of our simulations, RyR flux had to be converted from units of ionic current (i.e., number of ions per second, assuming a certain known concentration) to units of Ca^{2+} ions Molar^{-1} second^{-1} (i.e., ions per Molar per second, generalized to account for any concentration) according to Ohm's law. From this derivation, the number of ions per second that pass through a channel is expected to be directly proportional to the concentration of the ionic species. The single-channel current of the RyR, determined by Guo et al. (60), is 0.35 pA at a 1 mM concentration Ca^{2+} concentration in the SR. The current through an open RyR is converted to a rate, reflecting the number of Ca^{2+} ions released per second according to Eq. 4, below.

$$k_{RyR} = \frac{I^{RyR} 6.242 \times 10^{18} \frac{Charge}{Coulomb}}{[Ca^{2+}]z} = 1.09 \times 10^9 Ca^{2+} ions / s \quad (4)$$

Here, $I^{RyR} = 0.35$ pA, $[Ca^{2+}] = 1$ mM and $z = 2$, the RyR current, I^{RyR} in pA can be converted to charges using a conversion factor, $6.242 \times 10^{18} \frac{Charge}{Coulomb}$. Using a 1 mM concentration of Ca^{2+} in the SR and a charge on the ion $z = 2$ yields a rate of $1.09 \times 10^9 \frac{Ca^{2+} ions}{s}$ used for the flux of Ca^{2+} through an open RyR channel.

The user is provided with two models for RyR-Ca^{2+} gating: 1) a dual-state model of RyR (see Fig. 4 *b*) and 2) a multi-state model (see Fig. 4 *b*). In the dual-state model, RyR exists in an open or closed state (Fig. 4 *a*). Using a step-wise current, the user can modulate the duration time of the on and off states. In the closed state, the flux rate is set to zero until the activation time is reached. The user-modulated flux rate is then adjusted to k_{RyR} based on Eq. 4, above. When we validated our model, the pre-set termination times of the RyR opening were set in accordance with the experimental parameters to which we compared. Specifically, the studies by Hake et al. used an open-duration time of 28.5 ms (25), whereas the studies by Picht et al. and Brochet et al. used a duration of 100 ms (see Fig. S2).

More than 30 binding partners are known to interact with RyR (61,62). Thus, it is appropriate to model RyR as exist multitude of states. To reflect this complex behavior, we incorporated a well-established Markov model of RyR developed by Saftenku et al. (54). This model was used by Koh et al. in MCell simulations (34), further encouraging our choice to incorporate it into our model. The multi-state model is made up of a combination of closed (C) and open (O) and low (L) and high (H) gating modes (Fig. 4 *b*). The kinetic parameters for the RyR model (see Table S4) were used with little adaptation, with the exception of the RyR flux, which was increased by a factor of five to account for differences in mouse heart relative to the sheep hearts that were used to parameterize the original RyR model (63,64). In addition, state transitions and channel opening are governed by the ability of the receptors to bind Ca^{2+}. In this way, the user is able to model RyR in a way that responds to spatial encounters with Ca^{2+} in the dyadic cleft as the basis for its activation.

Modeling orphaned RyR2 with detubulation

Disease morphologies have been observed at the subcellular level in the form of deformities in T-tubules (8,65,66). This deformation results in an increased dyadic junctional space and a disruption of the couplon. Almost 20 years ago, Song et al. demonstrated that T-tubules bearing LTCC "move away" from SR membranes, effectively leaving "RyR clusters as functionally orphaned elements" (67,68). As our model is spatial in nature, we sought to recreate this phenomenon with the deformation of our TT geometry in the CRU. Others have studied these effects successfully (69). Fig. 5 shows how we increased our dyadic distance by three times (from 20 to 60 nm), resulting in roughly doubling the volume of the dyadic cleft (from $2.37 \times 10^{-3} \mu m^3$ to $4.69 \times 10^{-3} \mu m^3$), consistent with deformations made by others (67).

This deformation was performed manually in the Blender user interface. We selected TT2, pulling it down and away from the SR using the increase in dyadic volume as a guiding force. Once this was done, the deformed TT had escaped the cytosolic geometry. To maintain the integrity of the model, we curved the end of TT2 to ensure that it fit within the cytosol. Finally, the

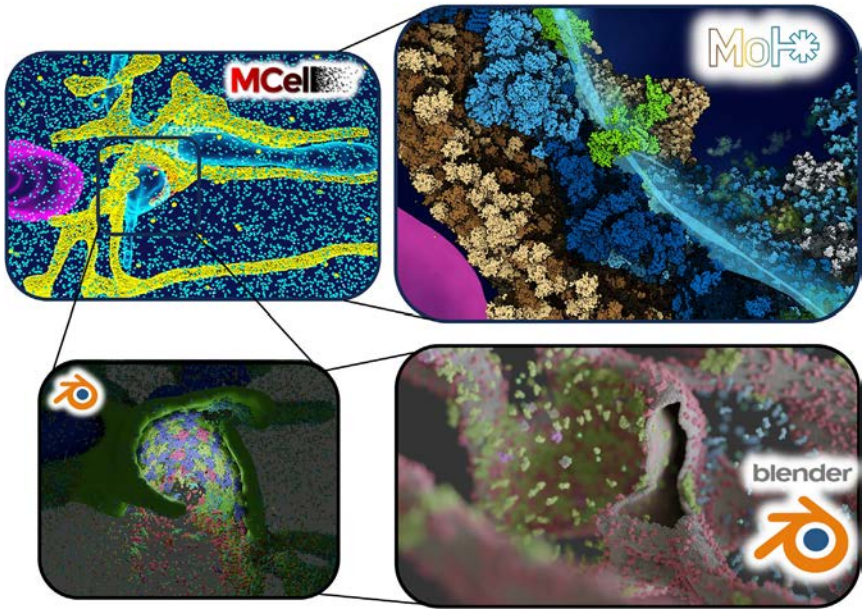

FIGURE 6 Model visualization with CellBlender, Mol ∗, and Molecular Nodes. Ways to visualize the output of MCell simulations. Top left: particle-species visualized with CellBlender showing mitochondria (*pink*), T-tubule (*transparent blue*), cytosolic Ca^{2+} (*large yellow spheres*), SR Ca^{2+} (*small yellow spheres*), and cytosolic buffers (*blue spheres*) created using MCell simulation. Top right: atomistic species visualized with Mol ∗ using atomic-level representations of molecules from the PDB. LTCC (*lime green*) is in the dyadic junction in close proximity with RyR (*dark/light blue and white*) and CSQN (*dark/light brown*) in the SR with the mitochondrial membranes displayed (*magenta*). Bottom left: Blender image of dyadic junction proteins rendered in atomistic representations in Blender showing RyR molecules in array of states (*lime*, *purple*, *blue*) juxtaposed with LTCC proteins (*ochre*, *red*, *teal*). Bottom right: cut-through image of the junction SR and surrounding proteins with atomistic representations (PMCA, *green*; SERCA, *pink*; NCX, *blue*; and lipids, *gray*) rendered with Molecular Nodes in Blender.

deformed TT intersected Mito1. As mitochondrial dynamics do not play an active role in our model, maintaining its structural integrity was not considered vital. We thus removed the intersecting regions and included a space between the TT and the mitochondrion for molecules to diffuse. The dyadic geometry can be modulated with an internal script that alters the dyad_geom_mode parameter in the CellBlender model. Explicit directions for how to execute this deformation can be found in the tutorial developed for our model in our repository (https://amarolab.ucsd.edu/hirakis.php).

Visualization of dynamics

Particle-species visualization with MCell CellBlender

To visualize the 3D positions of the MCell simulation, the user must choose which molecular species to visualize and how often to output their XYZ coordinates. These XYZ coordinates can be used to visualize the system in a myriad of ways (see Fig. 6). Within the Blender program, the user can import the visualization data and directly visualize the reaction-diffusion interaction within the CellBlender framework. Users have the ability to toggle the molecules that they wish to focus on to understand the spatial implications of their experimental setup. A video of RyR2 activation at the dyadic junction in response to a healthy AP is included in the supporting material (Video S1) and can also be found in our repository along with the model files (https://amarolab.ucsd.edu/hirakis.php).

Atomistic-species visualization

Spatial information about the 3D-positional data for molecular species outputted by MCell can be combined with atomistic structural details for better understanding of the molecular complexity of the system. An atomistic system can be generated by creating a system recipe (70), which maps molecular species to PDB identifiers (71) or custom atomistic structural files. This recipe can be used by cellPACKgpu (72), a program that generates 3D models by randomly placing molecular species in their respective compartments. It is important to note that atomistic representations are not simulated by MCell directly. PDB structures are applied to the position of molecules, and cellPACKgpu uses this to visualize the packing of the system. In the case of our system, the positions generated by the MCell trajectory are used to place the different species and play the simulation interactively. The user also has the option to view the fluorescence profiles of the trajectory, making for a direct comparison with fluorescence experiments (see Videos S2 and S3). We can then select any frame during the simulation and export a snapshot of the trajectory in a desired file format. If exported in mmCIF file format, the MCell simulation snapshot can be interactively explored in atomistic molecular viewers (see Videos S4 and S5) such as the mesoscale explorer based on Mol∗ (73) (https://mesoscope.scripps.edu/explorer/). Alternatively, mmCIF or other file formats can be imported into Blender and visualized using Molecular Nodes for more advanced rendering techniques (https://bradyajohnston.github.io/MolecularNodes/). This approach provides users with a more detailed and realistic view of the packing of such biologically complex systems, which facilitates the creation of images and animations using the XYZ particle positions outputted by MCell (see Fig. 6). However, it is important to note that this visualization method does not correct for potential steric clashes resulting from close particle contacts in MCell trajectories. mmCIF models of the peak Ca^{2+} levels for both healthy and deformed systems are also made available in the repository associated with this model (https://amarolab.ucsd.edu/hirakis.php).

RESULTS

Model validation

Dual-state RyR model

To validate our model output, we compared our stochastic particle system with in silico modeling experiments, as well as in vitro imaging experiments. As a first step, we chose to recreate the phenomenological sparks and fluorescence recovery patterns produced by Hake et al. upon which this model was first based. In these studies, a system of ordinary and partial differential equations (ODEs/PDEs) was used to describe the behavior of the molecular species in the CRU. The sparks generated were phenomenological in which a set number of RyRs were set to open for a specified period of time. In our system, RyR Ca^{2+} efflux was achieved using the formerly described dual-state RyR model. Specifically, five RyR molecules placed in the

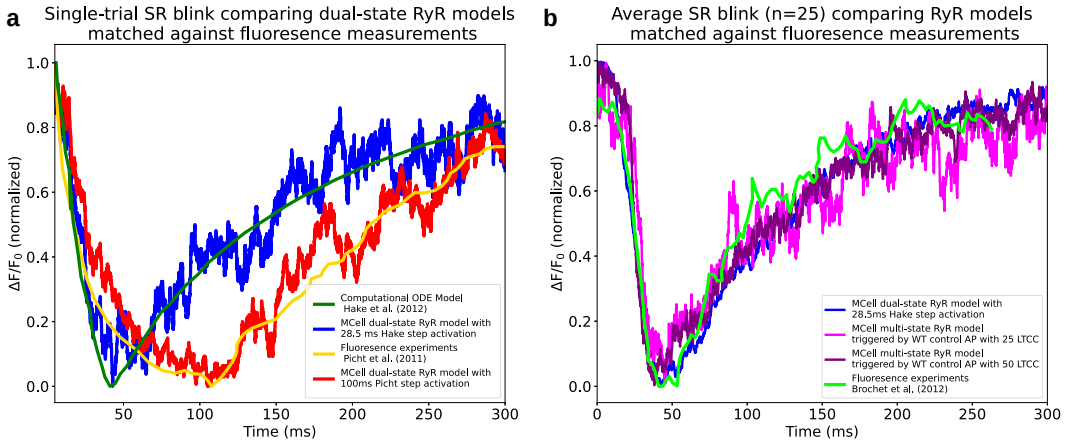

FIGURE 7 Model validation: SR blink behavior of MCell model compared with fluorescence measurements. (*a*) Single-dyadic-junction SR refill profiles of the deterministic computational model (*green*), data from Hake et al.; MCell dual-state RyR model with Hake stimulus (termination time 28.5 ms, *blue*); fluorescence experiments by Picht et al. (*gold*); MCell dual-state RyR model with Picht's stimulus (termination time 100 ms, *red*). (*b*) The average dyadic SR calcium depletion comparing MCell dual-state RyR model with step-current (*blue*) MCell multi-state RyR model with 50 LTCC and WT control AP (*purple*), MCell multi-state RyR model with 25 LTCC and WT control AP (*magenta*), and fluorescence experiments by Brochet et al. (*lime green*).

junctional SR membrane were set to open with a Ca^{2+} flux equal to k_{RyR} (see section "materials and methods," Eq. 4) for a given duration (see Fig. S2). The behavior of the dual-state model was compared with two experiments: 1) the computational ODE/PDE model by Hake et al. with a step activation time of RyR of 28.5 ms (25); 2) fluorescence measurements by Picht et al., with a step activation duration of RyR of 100 ms (44) (see Fig. S2). As reflected in Fig. 7 *a*, stochastic experiments with MCell (blue) matched the SR Ca^{2+} blinks observed in experiments by Hake et al. well. By simply adjusting the termination time to 100 ms (red), the dual-state RyR model reproduces the Picht et al. in vitro fluorescence SR blink measurements. Together, these results demonstrate the ability of the dual-state RyR MCell model to reproduce observations made using deterministic computational methods as well as imaging experiments in tissue.

Multi-state RyR model

The motivation for implementing a multi-state RyR model is based on the multitude of molecular players with which RyR can interact (62). Furthermore, we sought to develop a model of CICR that could sense and respond to even the slightest local changes in dyadic Ca^{2+}, allowing us to model more complex disease states, such as alterations in disease APs (74). Others have shown the importance of RyR being able to respond to nanoscopic changes in Ca^{2+} concentration (63). As such, we decided that this was of utmost importance to consider in our spatial model. Finally, we sought to develop a model that could reflect the complex behavior of this system and was capable of both triggered and spontaneous activation.

To validate the behavior of our multi-state RyR model, we matched the model output to fluorescence experiments. As experiments by Picht et al. and Hake et al. directly influenced the construction of our model, we chose to compare our multi-state model behavior with fluorescence blinks performed by Brochet et al. (75). We compared MCell systems with 50 and 25 activatable LTCCs and the multi-state RyR model to imaging experiments by Brochet et al. as well as our dual-state RyR model (see Fig. 7 *b*). The control AP by Wang et al. was used to activate LTCCs resulting in triggered CICR. The behavior of all of our models adequately matches the independent experimental SR blink behavior. Because the behavior of 25 and 50 LTCCs produced relatively similar activation profiles, we thought it best to use the lower of the two numbers. As such, all experiments discussed in the results are those that incorporate 25 LTCCs. This demonstrates that the CICR MCell model agrees well with established behavior reflected in experiments not used to directly parameterize our model.

The inclusion of the stochastic multi-state model of the RyR not only affords the ability to sense increases and dyadic Ca^{2+} and trigger Ca^{2+} efflux as a response, but also gives RyR the ability to spontaneously activate. As shown in Fig. 8, the multi-state model is capable of spontaneous RyR firing in the absence of triggering APs. This is an important feature of the multi-state RyR model. The spontaneous RyR firing events are relatively infrequent, as suggested in the literature (2,76), occurring only sparingly in our simulated systems. This important feature makes this model valuable to those seeking to study RyR leaks that contribute to arrhythmogenic behaviors. An important distinction: this RyR model has only been parameterized for CICR. The model will require further exploration and parameterization for the production of non-triggered spontaneous sparks. However, this model provides a viable starting point for researchers eager to do so.

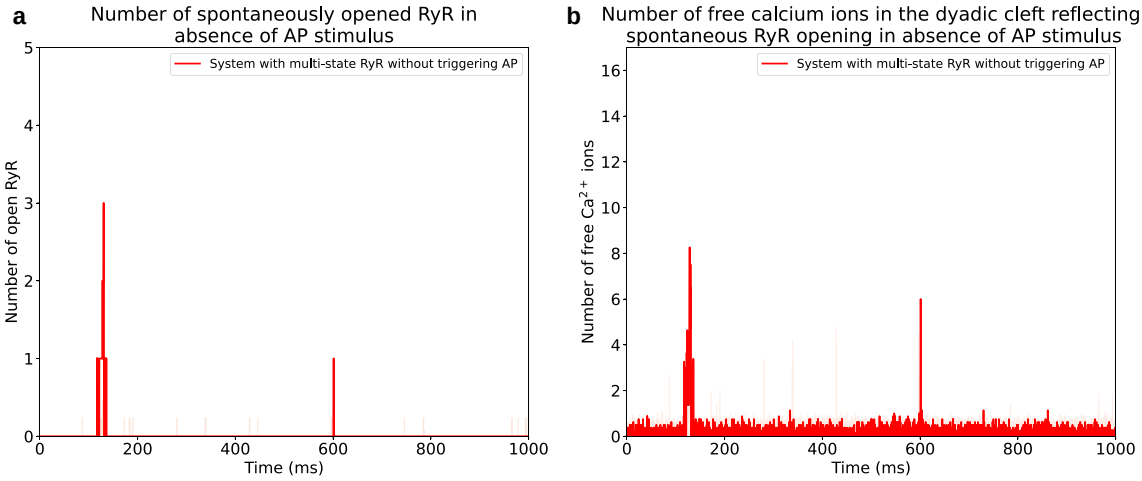

FIGURE 8 Spontaneous activation of RyRs. (*a*) Number of spontaneously opened RyRs in absence of AP stimulus. (*b*) Number of free Ca^{2+} ions in the dyadic junctional space. Solid lines denote single trial measurements, and shaded colored region denotes standard deviation of the mean.

AP-driven calcium release

An important distinction in this modeling framework is the number of activatable receptors available vs. the number of receptors actually activated during an AP. Practically, this means that not all receptors will fire because of the stochastic nature of the simulations. Moreover, it means that the systems will have a different arrangement of receptors that are activated each time. Referring to Fig. 9, we see that systems with 50 activatable LTCCs activate approximately 15 LTCCs during the peak of the AP in the absence of RyRs, a population activation of approximately 30%. Similar population activation fidelity is observed in systems that contain 40, 25, and 10 activatable LTCCs. In all cases, the number of Ca^{2+} ions is tightly controlled by SERCA and buffer species, especially in the dyadic junction. In general, the relative contribution of LTCCs to overall Ca^{2+} levels is low compared to systems that contain RyRs. This is an important and novel result observed in our encounter-based model. Deterministic modeling systems can exhibit fractional LTCC population firing only if explicitly parameterized to do so.

The present model is sensitive to changes in the AP input. In experiments in which the APs are altered from control (WT-sham) to disease models (WT-TAC), the system produces different CICR behaviors that are immediately apparent at the molecular level (see Figs. 10 and S3). Both LTCCs and RyRs have distinct and detectable differences in activation behavior when the AP is altered (see Fig. 10 *e* and *f*). Specifically, the LTCC current decreases significantly and rapidly after depolarization in the case of diseased AP systems. This results in a slightly dampened CICR response that is readily detectable in our systems but may not be apparent in in vivo and in vitro experimental systems, not yet sensitive enough to detect such slight changes in concentration at this microscopic spatial and temporal scale.

In the present model, the user can visualize RyR activation patterns at resolutions not yet available with modern imaging techniques (see Video S1). Visualizing the opening of RyRs in real-time in response to AP triggering is of great importance for understanding the mechanism of CICR action. The most important feature taken from this model are the cluster-pattern firing of as RyRs. Videos of RyR firing patterns can be found in the Supporting Material generated by MCell as well as cellPACK/Mol*. This result is one of the most interesting products of this model and it is our hope that the greater modeling community will use and fully appreciate this novel ability to visualize this unseen phenomenon.

T-tubule deformation and its effects on local control

Simulating encounter-based reaction systems sets the groundwork for an important application of this model to understand how membrane deformations can affect CICR (77). The spatial dispersion of T-tubules has been shown to result in orphaned RyRs that cannot propagate a Ca^{2+} signal (67). The couplon is disrupted with an increase in the LTCC-RyR distance, and local control is lost. We sought to use our model to test this hypothesis of an increase in the dyadic distance and specifically examine the effects on the resulting CICR.

As shown in Fig. 10, the effects of the TT deformation are readily apparent in all aspects of CICR. Although LTCCs successfully activate in all cases according to their APs (Fig. 10 *c* and *e*), RyRs fail to open in the case of the deformed TT. Of the 96 RyRs present to be activated, healthy TT systems will activate a quarter of the receptors, roughly 20% at the peak of the AP (see Fig. 10 *d*). In contrast, deformed systems will activate roughly 1% of the RyR as a result of detubulation. The resulting RyR Ca^{2+} flux rate is very low, demonstrating the ways in which local control is lost.

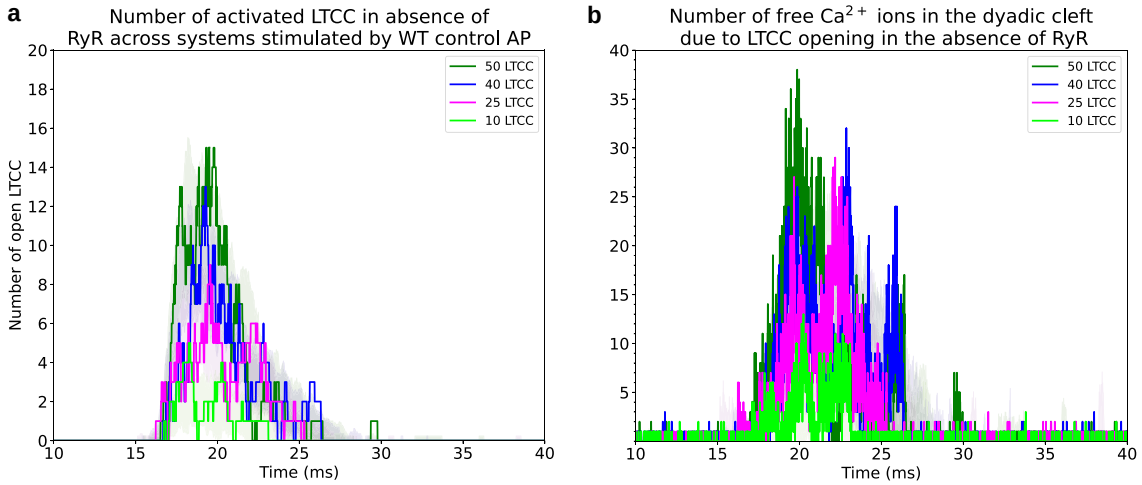

FIGURE 9 Activation behavior and cytosolic Ca^{2+} contribution of LTCCs. (*a*) Comparison of number of activated LTCCs in absence of RyRs across systems stimulated by WT control AP. (*b*) Number of free Ca^{2+} ions in dyadic cleft reflecting LTCC opening in absence of RyRs. Color correspondence: 50 LTCCs (*green*), 40 LTCCs (*blue*), 25 LTCCs (*magenta*), and 10 LTCCs (*lime green*). Solid lines denote single trial measurements, and the shaded region denotes the standard deviation of the mean.

The highest free Ca^{2+} of all systems (Fig. 10 *a*), total Ca^{2+} (Fig. 10 *b*), RyR activation (Fig. 10 *d*), and RyRCa^{2+} influx (Fig. 10 *f*) was exhibited by the healthy TT with control AP system. The deformed TT results in a nearly complete failure to activate RyRs, as has been shown by others (78). Mirroring the case of healthy TT, diseased AP has a shorter duration of Ca^{2+} flux in deformed TT (Fig. 10 *f*). Taken together, the observed effects are directly explained by the close physical contact of LTCC and RyR in the case of the healthy T-tubules. The tighter physical coupling of LTCC and RyR translates to a shorter distance traveled by Ca^{2+} when entering the cell through an LTCC. This result is only evident in the case of the multi-state RyR, which senses local changes in Ca^{2+} concentration to fire, whereas the phenomenological, dual-state RyR model will fire regardless of the change in dyadic distances.

RyR cluster firing and variability in calcium spark generation

One major advantage of stochastic simulations is the ability to investigate the inherent variability in the behavior of a system. It is known that only a fraction of calcium release units will activate in response to an AP (29). This is most evident when analyzing the frequency within which events occur between the different trial seeds, and when comparing the different systems against each other. In these cases, an average is less informative than viewing the range of behaviors observable in the system, which are widely variable within the same system.

The deformation of the T-tubule has a marked effect on the generation of Ca^{2+} sparks in response to APs (Fig. 11 *a* and *c*). Approximately 60% of healthy TT systems respond to the AP with a spark generated, whereas only 25% of deformed TT systems will generate a spark in response to the control AP (Fig. 11 *a*). Healthy TT and control AP systems exhibit the greatest degree of system variability, showing how frequently a system can activate RyR clusters. Deformed TT systems lose this variability and fewer RyRs are activated, thus leading to la reduced probability in Ca^{2+} spark generation. When the AP is diseased, the decrease in Ca^{2+} spark fidelity is even more pronounced. With a diseased AP, 25% of healthy TT systems will generate sparks, and, in the case of deformed TT and disease AP, the system completely loses the ability to generate calcium sparks. Said differently, the deformation of the TT leads to the loss of system variability in the number of RyRs that can be activated in response to an AP, effectively knocking out the ability of the system to property activate.

Calcium spark fidelity is inextricably linked to the activation of RyR clusters. We consider a calcium spark as being attributed to four or five RyRs opening in response to an LTCC-triggered event, consistent with Hake et al., who used five RyRs to elicit their sparks. In terms of the number of free Ca^{2+} ions and bound Ca^{2+} species, this corresponds to RyRs amplifying the amount of Ca^{2+} let in by LTCC by 2.5 times. This threshold is designated as a gold line in Fig. 11 *a* and *c* to denote differences in Ca^{2+} spark generation between the systems. In the case of healthy TTs (Fig. 11 *a* and *e*), there are several clusters of RyRs activated to produce a calcium spark. This is in stark contrast to deformed TTs (Fig. 11 *c* and *f*), where RyRs are more likely to fire as individual channels within the junction. That is, when the couplon is disrupted by deformation, the enlarged dyadic junction allows Ca^{2+} to diffuse away from neighboring RyR within the clusters, resulting in the aforementioned phenomena of orphaned RyRs. In the case of healthy TTs, the diffusion of Ca^{2+} is restricted to a smaller space due to the closely juxtaposed TT. When LTCCs open in healthy dyadic junctions, the TT acts as a physical barrier,

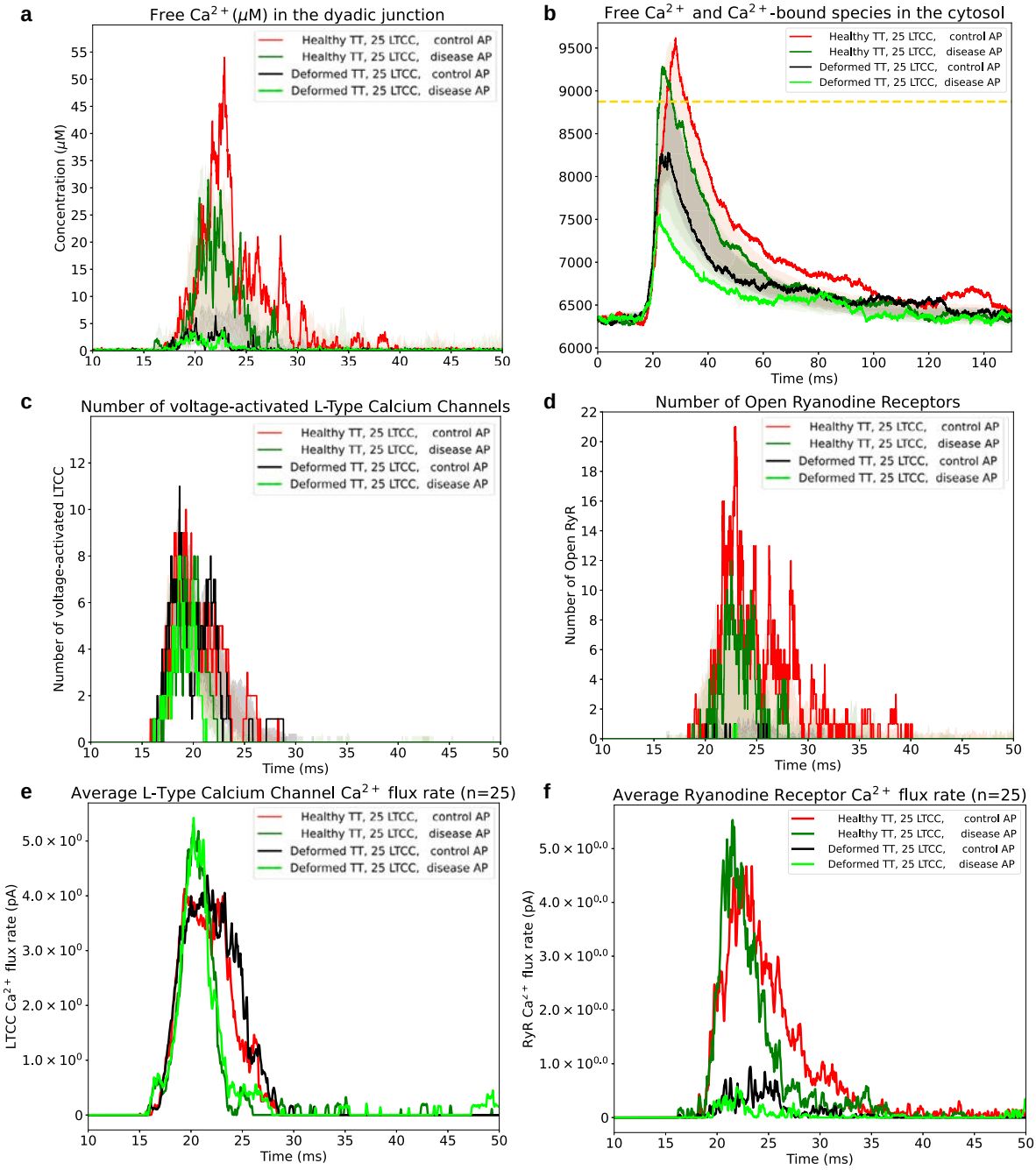

FIGURE 10 Comparison of system behavior when altering APs and T-tubule geometries. (*a*) Concentration of free Ca^{2+} in the dyadic junction. (*b*) Number of free and Ca^{2+}-bound species in the cytosol. (*c*) Number of voltage-activated LTCCs. (*d*) Number of open RyRs. (*e*) Average LTCC Ca^{2+} flux rate ($n = 25$). (*f*) Average RyRs Ca^{2+} flux rate ($n = 25$). Solid lines denote single trial measurements, and shaded colored region denotes standard deviation of the mean. Systems with 25 LTCCs: healthy T-tubule, control AP (*red*); healthy T-tubule, disease AP (*green*); deformed T-tubule, control AP (*black*); deformed T-tubule, disease AP (*lime green*). Dashed gold line in (*b*) denotes the calcium spark threshold.

restricting the movement of calcium ions within the junction. Calcium is thus more likely to bind to a neighboring RyR within the space, resulting in neighboring RyRs being activated in a cluster formation (Fig. 11 *e*). This can be observed when viewing the visualizable simulation output (see Videos S1 and S2). In the case of deformed TT, the volume of the dyadic junction is increased, and the resulting enlarged dyadic volume no longer restricts the Ca^{2+} entering the junctional space. Our spatial particle simulations demonstrate how Ca^{2+} ions diffuse within the junction upon being released from the SR (Video S3). The larger path of diffusion in deformed TT morphologies results in lower numbers of RyRs activated throughout the dyadic junction (Fig. 11 *b* and *d*). In general, deformed TTs result in single

channel activations (Fig. 11 *f*) as opposed to RyR cluster pattern activation in healthy TTs (Fig. 11 *e*).

DISCUSSION

In the present work, we use realistic geometries to create a stochastic, encounter-based model of cardiac Ca^{2+} signaling that reflects biological variability and complexity. By modeling the important molecular species that underlie Ca^{2+} signaling using particles, molecules must encounter each other in physical space to react with one another. By modeling cardiac Ca^{2+} signaling in stochastic spatial models, we are able to tease out the factors that underlie local control in healthy systems and disrupt CICR in disease morphologies.

The greatest challenge in studying the cardiac system is the integration of multiscale models (79) in ways that can capture the complexity of the structure and function of the heart. Moreover, computational models are able to test hypotheses that are difficult to study with other traditional methods. In such cases, computational models of the heart have played an important role in illuminating the processes that underlie cardiac function and dysfunction (80). The field of computational cardiology almost exclusively uses continuum approaches to model the dynamics of cardiac systems. Despite this, several cardiac scientists have called for discrete modeling of cardiac Ca^{2+} dynamics. Maleckar et al. stated that "the restricted number of molecules in each CRU can mean that approximating dynamics as continuous is inappropriate: processes therein may be better described by stochastic models as opposed to deterministic models" (4). Cheng said that "at the molecular level, transmembrane Ca^{2+} translocation should be considered a discrete, stochastic process," (36). Finally, Bers said "we may also have to start thinking more stochastically about local reactions. For example, at resting $[Ca^{2+}]_i$ there is less than one free Ca^{2+} ion in an entire junctional cleft, making the concept of collision probability more meaningful than concentration" (28). It is the low numbers of Ca^{2+} ions at rest that make discrete modeling a well-suited method for studying this process. This study has demonstrated the ways in which the physical location of a small number of Ca^{2+} ions plays an important role in Ca^{2+} activation.

Computational cardiac Ca^{2+} modeling has a productive history that spans three decades (17) and has provided an understanding of both cardiac function and dysfunction by making it possible to experiment with specific subcellular phenomena (3,27). The inner workings of the cardiac myocyte system are, as in most cellular systems, extremely intricate and complex. Using powerful computational tools that can build and examine systems more holistically and realistically (25,26), researchers can now contextualize findings and answer questions that are difficult to ask experimentally in vivo and in vitro.

The computational discretization of the CRU system is an important advance in modeling CICR (28). Due to the extremely low resting level of Ca^{2+} in the CRU (140 nM), small changes in the tightly controlled cardiomyocyte activation process can have major effects. Upon discretization of the single CRU, we estimate that there is, at rest, an average of 35 free Ca^{2+} ions in a cytosolic volume of 0.424 μm^3, and, of those, roughly zero to three ions on average are located in the region of the dyadic cleft (see Fig. 9 *b*; Table S6). Due to the low number of ions at rest, the present model, which describes the discrete spatial location of Ca^{2+}, is more representative of biological reality than a continuum representation based on concentration and probabilistic location (4,28).

Incorporation of an RyR model that describes the ability to be activated and inactivated by Ca^{2+}, as well as a model of LTCCs that are both calcium and voltage dependent in activation, makes this a computational model well-suited to model the phenomenon of CICR. In this way, we are able to stimulate LTCCs using AP models and observe the response of RyRs to this activation. Thus, sparks are self-generating and self-terminating, addressing the limitations of the earlier model by Hake et al. (25). Of added importance is the model's capacity not only to produce AP-induced sparks in response to LTCC stimulation but also to produce spontaneous, non-triggered sparks.

Our model reproduces imaging experimental results such as SR Ca^{2+} blinks, ensuring that model behavior is consistent with already-understood behaviors. Furthermore, we confirm that typical sparks result from the activation of fewer RyRs ($\sim$20) than those actually present at the dyadic junction (81). This result is also true for LTCCs, whose actual activation numbers reflect only a fraction ($\sim$10 LTCCs activated) of the 25 LTCCs present.

These experiments, however, provide an additional insight into LTCC activation of RyRs. The model suggests that roughly 25–50 activatable LTCCs are required to elicit an effective CICR response based on simulations with the 96 RyRs originally imaged by Hayashi in this exact geometry (24,40). An important distinction here is the number of receptors present vs. the number of receptors activated. As stated previously, only a fraction of the LTCCs and RyRs present actually activate in any given case. Moreover, the activation of RyRs is not guaranteed. We observe cases in which RyR activation is not triggered by LTCC action. This is fully consistent with observations in the literature (29,82), making us more confident in our model's ability to mimic biological reality.

Our experiments indicate that a ratio of RyRs to LTCCs of approximately 4:1 is required to trigger CICR. By increasing the number of LTCCs in the junctional T-tubule, we observed an increase in the overall Ca^{2+} flux rates of RyRs. The multi-state RyR model responds with positive gain to the LTCCs activated in response to

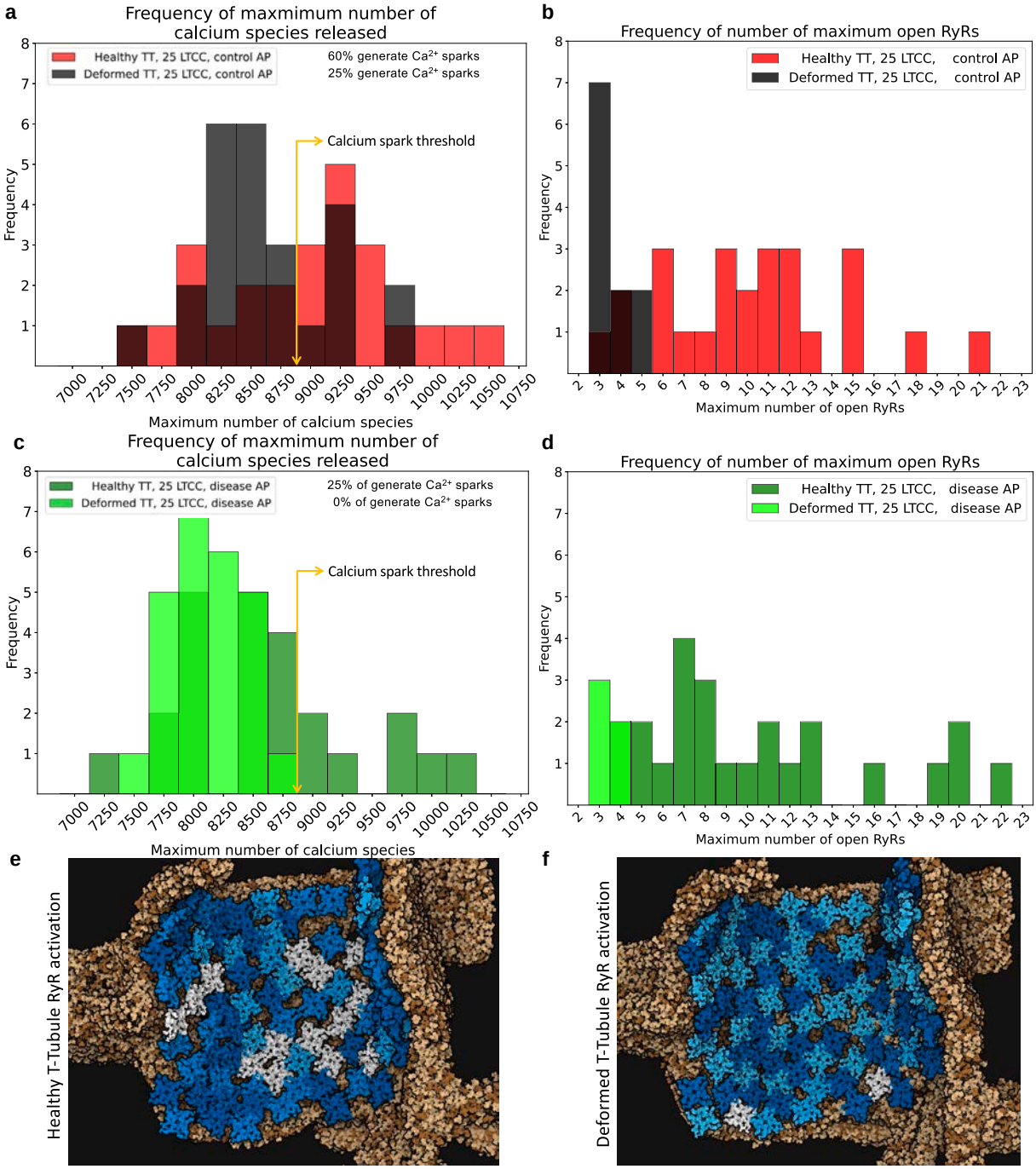

FIGURE 11 Variability among maximal calcium and number of open RyRs across systems. (*a*) Maximal Ca^{2+} released in systems with control APs. (*b*) Maximal number of open RyRs in systems with control APs. (*c*) Maximal Ca^{2+} released in systems with disease APs. (*d*) Maximal number of open RyRs in systems with disease APs. Systems with 25 LTCCs: healthy T-tubule, control AP (*red*); healthy T-tubule, disease AP (*green*); deformed T-tubule, control AP (*black*); deformed T-tubule, disease AP (*lime green*). (*e*) Healthy T-tubule RyR activation patterns. (*f*) Deformed T-tubule RyR activation patterns; open RyR (*white*); closed low-gating RyR (*light blue*); closed high-gating RyR (*dark blue*); CSQN in SR (*brown and tan*); images made with Mol* server.

an AP, and 25 LTCCs are shown to be sufficient to activate the 96 RyRs observed in this particular dyadic junction.

Diseased states such as trans-aortic constriction produce altered APs, which can be used in our system to stimulate our activatable LTCCs in the junctional TT. Our simulations produce subcellular observations consistent with experiments, reflecting lower systolic Ca^{2+} upon excitation with disease AP compared to control AP. This is a promising result, making a case for the ability of our model to tease

out differences in Ca^{2+} handling within a single CRU system as a result of altering the AP.

The extensive work to design an explicit species model for cardiac Ca^{2+} modeling took several years of careful development and experimentation. The power of this easily usable model, complete with system preparation analysis scripts, can be applied directly to systems to investigate subcellular effects in interesting new geometries, altered membrane morphologies (77), and channel defects found in disease states (83). In the case of the present study, we used detubulation to model physically observable markers of heart failure as a way to study the alteration in the geometry of CRU and its role in CICR.

In the present work, the value of an explicit-particle spatial and stochastic model is most evident when considering the activation patterns of RyRs in the dyadic junction. The cluster-firing of RyRs in the junction is only observed in healthy TT systems, due to the restricted volume within which Ca^{2+} can diffuse. Our experiments suggest the underlying phenomenon responsible for failed CRU activation in detubulated geometries is the inability of RyR to activate in clusters as is seen in healthy hearts. In such cases, the user of this model can investigate the patterns of RyR activation in clusters versus single RyRs that activate in deformed TT systems. The videos included in our Supporting Material provide a visual perspective of CICR, which is one of the most novel products of this work. In the present literature, no similar perspective is offered to those seeking to computationally understand CICR at the level of single Ca^{2+} ions and proteins. The user has the option to view the system players as particles (MCell and CellBlender) or atomistically described in a volumetric model of the CRU (cellPACK and Mol∗). Finally, the variability observed in the CICR process that is lost in deterministically designed systems can be readily observed in our stochastic system. The present model faithfully reproduces the behavior of cardiac myocytes, which are known to activate only fractionally in response to an AP stimulus and spontaneously in its absence.

Although we model a single CRU, the true power of the model is its ability to simulate systems with different geometries and to be applied to tomographic reconstructions of multiple CRU systems. This model can be applied to any geometry, whether simplified or realistic. The number of important membrane channels and receptors is modular and can be adjusted to model a variety of cardiac diseases. Moreover, using the computational tool of MCell allows us to look at the distribution of molecular species in *specific* regions of interest such as the dyadic cleft and the junctional SR. Our experiments investigate single-AP dynamics, but sequences of APs have been tested in the model, simulating a beating heart (84).

Important limitations of the model must be addressed to further improve the predictions and usability of the model. Neither the model originally created by Hake et al. nor the presently described model includes important adrenergic regulators (85), such as calcium-calmodulin kinase II (CaMKII) (86), inositol triphosphate receptors (87,88), and protein kinase A (6,89,90), known to regulate important players in the CICR process already included in our model (such as RyR). However, our model is easily adapted to include these and other important molecules, as was done by Yang et al. using MCell with cyclic adenosine monophosphate (91). However, experimental observables (such as AP alterations (92)) resulting from diseased states in molecules not captured in our model can also be included, resulting in similar experimental observables (84).

Further limitations include the absence of the dynamics of the mitochondrial system (93). A recent model of mitochondrial dynamics produced in neuronal synapses (94) presents an important opportunity for such a model to be integrated, adapted, incorporated, and investigated in the context of cardiac systems. Furthermore, because our model features only a portion of the SR network, it cannot answer the questions about global depletion of SR Ca^{2+}. With the ability to apply the dynamics to larger systems featuring more extensive SR networks, this limitation will be mitigated. Important advances in mouse myocardial imaging can then be used to compare the predictions made by our model with systems in situ and in vitro.

Undoubtedly, computational power will increase sufficiently in the near future so that the volumetric and energetic components of molecular species can also be included in models that seek to include as much molecular detail as possible (95). Importantly, RyRs have been shown to be able to reorganize within the dyadic junction, especially in diseased morphologies (96–99), and even exhibit alterations in phosphorylation (100,101). Without the inclusion of energetic or volumetric components in our model, we cannot accurately model this phenomenon. Furthermore, electrostatic forces (102) surely play a role in the diffusion path that Ca^{2+} takes when introduced into the system through LTCCs and in binding to RyRs. The lack of electrodiffusion as a biasing force in the reaction between molecules is an admitted limitation of our model. Moreover, the lack of volumetric components of molecular species introduces possible packing and steric clash errors, as shown by the use of cellPACK to model the atomistic representations of the species. This means that molecules can artificially overlap because MCell lacks volume and orientation components when treating molecules as particles. As MCell and other tools further develop to account for these important factors, we will converge on models that more accurately reflect biological reality.

Furthermore, imaging studies have detected a large variability in the size of the CRU and therefore the number of RyRs in dyadic junctions (24,40,96). Our system is an admittedly large CRU, containing 96 RyRs that were counted in the original segmented images, falling on the larger side of the range of sizes that have been observed.

As our model is easily applicable to different geometries, it is our hope that the greater modeling community will use this framework to investigate the dynamics of a variety of CRUs. A present limitation to this prospect is the number of segmented geometries available for public use. With the advent of machine learning, the intensively laborious process of manually segmenting images and correcting them will undoubtedly simplify, resulting in geometries that are more plentiful and therefore, readily accessible to the cardiac modeling community as a whole (103).

Scientists who would like to understand and visualize a biological process can use MCell to design a model with the language of biochemical reaction schema without requiring specification in the formal language of ordinary and/or partial differential equations to describe system dynamics. This model will appeal to researchers outside the mathematics/physics/engineering backgrounds, which encompass the large majority of scientists that use ODE/PDE modeling regimes (104). In steep concentration gradient changes, PDE methods require finer and finer spatial decomposition to the point where the volumes of the tiny compartments are so small that they would contain only a few molecules, invalidating the continuum assumption. In such systems, a particle-based approach is most appropriate. This occurs specifically within the space of the dyadic junction, where the concentration of Ca^{2+} is extremely low at rest. In our simulations, we see between zero and three free Ca^{2+} ions at steady-state (see Table S6). This rapidly changes when LTCCs open in response to an AP and when RyRs are activated as a result. In such cases, continuum dynamics become less appropriate to model the rapid and steep changes in Ca^{2+} concentration at short timescales. Finally, if researchers would like a way to visualize their output in a particle-based or atomistic way, they may use our model visualization techniques.

Looking toward the future, this work can potentially be combined with cryo-electron tomography (cryoET) images of subcellular volumes (105). Using MCell to model the dynamics of molecular species and cellPACK to pack the volume with the appropriate species is a very tangible and straightforward way to link cryoET images with investigations of biological function (106). We envision a pipeline of subcellular images from cryoET and TEM that can connect with higher-resolution images of protein species in cellular cryoelectron microscopy and crystallography. It is not beyond reach to interface this model with that of Stevens et al., who first embarked on the challenge of simulating a whole cell in atomistic detail (107). The ultimate vision of multiscale modeling is the ability to model and examine the same system at multiple disparate levels (6,7). Our method presents a very real way to achieve this milestone, bridging the subcellular and molecular scales directly. We believe this new method will prove valuable to modelers and nonmodelers alike; that the insights gained from this work will be useful to the cardiac Ca^{2+}-handling community, and scientists who wish to use a similar modeling regime for their own systems.

CONCLUSIONS

We have developed a model of subcellular cardiac Ca^{2+} dynamics and describe the study of realistic cardiac geometries using approaches that track the explicit spatial locations of molecular species. We have incorporated Ca^{2+}-handling species that treat Ca^{2+} explicitly to accurately account for the location and number of Ca^{2+} ions during activation processes. To study couplon dynamics, we include LTCCs that activate in response to an AP and RyRs that activate in response to spatial interactions between Ca^{2+} ions and individual channels. In the absence of an activating AP, this model produces spontaneous RyR openings, providing a viable starting point for those who seek to study non-triggered Ca^{2+} spark leak behavior at the single-molecule level. In focusing on disease morphologies in orphaned RyRs, we see that RyRs are more likely to activate in clusters in healthy TT morphologies and in detubulated systems, as individual receptors, incapable of activating one another. Finally, this model provides a way for scientists to visualize firing patterns of RyR clusters in multiple rendering modes. With the development of this model and the usage materials made available to the reader, we have the sincerest hope that the cardiac modeling community will use and further develop the CRU model we have designed to answer more outstanding questions in cardiac function and disease.

ACKNOWLEDGMENTS

The authors thank Dr. Johan E. Hake for providing us with the CRU geometry and his advice as we started our project. We graciously thank Dr. Andrew McCulloch and Andrew G. Edwards for their advice on model construction. The authors thank our mentor and colleague, Dr. Katja Lindenberg, for her tireless guidance and challenges as the model was created. We graciously thank Dr. David D. Thomas and Dr. J. Michael Autry for their communication with regard to the SERCA model. The authors thank Robert Kuczewski and Dr. Adam Husar for their invaluable support and development of CellBlender and MCell. In addition, we thank Dr. John (Jack) Berkowitz and Ray Arvin C. Rimorin for their support in the analysis of the results. We also graciously thank Dr. Brady Johnston for his help in rendering images with Molecular Nodes. Finally, this work is dedicated to the memory of our beloved colleague, Anouchka Mihaylova (Anushka Michailova). S.P.H. was funded through a fellowship from the Interfaces Graduate Training Program (NBIB T32 EB009380). The research was funded in part by the National Institutes of Health (NIH) through the NIH Director's New Innovator Award Program (DP2-OD007237 to R.E.A.) and an NSF XSEDE/ACCESS supercomputer resources grant (CHE060073N to R.E.A.) from the National Biomedical Computation Resource (NBCR) and the NIH P41 GM103426. L.A. is supported by NIH grant R01GM120604. Modeling was also supported by NIH MMBioS P41-GM103712, NSF NeuroNex DBI-1707356, and NSF NeuroNex DBI-2014862 to T.J.S.

AUTHOR CONTRIBUTIONS

S.P.H. and T.M.B. designed the research. S.P.H. carried out all the simulations and analyzed the data. L.A. and T.M.B. assisted in the visualization of the system output. S.P.H. wrote the article with the help of T.M.B., L.A., T.J.S., and R.E.A., who also advised the research.

DECLARATION OF INTERESTS

The authors declare no competing interests.

SUPPORTING MATERIAL

Supporting material can be found online at https://doi.org/10.1016/j.bpj.2024.09.029.

REFERENCES

1. Ahmad, F. B., and R. N. Anderson. 2021. The Leading Causes of Death in the US for 2020. *JAMA.* 325:1829–1830.
2. Sutanto, H., A. Lyon, …, J. Heijman. 2020. Cardiomyocyte calcium handling in health and disease: Insights from in vitro and in silico studies. *Prog. Biophys. Mol. Biol.* 157:54–75.
3. Niederer, S. A., J. Lumens, and N. A. Trayanova. 2019. Computational models in cardiology. *Nat. Rev. Cardiol.* 16:100–111.
4. Maleckar, M. M., A. G. Edwards, …, G. T. Lines. 2017. Studying dyadic structure-function relationships: A review of current modeling approaches and new insights into Ca2+(mis)handling. *Clin. Med. Insights Cardiol.* 11:1179546817698602.
5. Bartol, T. M., D. X. Keller, …, M. B. Kennedy. 2015. Computational reconstitution of spine calcium transients from individual proteins. *Front. Synaptic Neurosci.* 7:17.
6. Boras, B., S. P. Hirakis, …, A. D. McCulloch. 2015. Bridging scales through multiscale modeling: A case study on protein kinase A. *Front. Physiol.* 6:250.
7. Colman, M. A., E. Alvarez-Lacalle, …, J. Heijman. 2022. Multi-Scale Computational Modeling of Spatial Calcium Handling From Nanodomain to Whole-Heart: Overview and Perspectives. *Front. Physiol.* 13:836622.
8. Ibrahim, M., J. Gorelik, …, C. M. Terracciano. 2011. The structure and function of cardiac t-tubules in health and disease. *Proc. Biol. Sci.* 278:2714–2723.
9. Ferrantini, C., C. Crocini, …, L. Sacconi. 2013. The transverse-axial tubular system of cardiomyocytes. *Cell. Mol. Life Sci.* 70:4695–4710.
10. Tran, D. B., C. Weber, and R. A. Lopez. 2024. Anatomy, thorax, heart muscles. *In* StatPearls [Internet] StatPearls Publishing.
11. Lu, X., L. Xu, and G. Meissner. 1994. Activation of the skeletal muscle calcium release channel by a cytoplasmic loop of the dihydropyridine receptor. *J. Biol. Chem.* 269:6511–6516.
12. Stern, M. D., L. S. Song, …, E. Ríos. 1999. Local control models of cardiac excitation-contraction coupling. A possible role for allosteric interactions between ryanodine receptors. *J. Gen. Physiol.* 113:469–489.
13. Stern, M. D. 1992. Theory of Excitation-Contraction Coupling in Cardiac-Muscle. *Biophys. J.* 63:497–517.
14. Cheng, H., W. J. Lederer, and M. B. Cannell. 1993. Calcium sparks: Elementary events underlying excitation-contraction coupling in heart muscle. *Science.* 262:740–744.
15. Cannell, M. B., H. Cheng, and W. J. Lederer. 1994. Spatial non-uniformities in [Ca2+]i during excitation-contraction coupling in cardiac myocytes. *Biophys. J.* 67:1942–1956.
16. Cannell, M. B., H. Cheng, and W. J. Lederer. 1995. The control of calcium release in heart muscle. *Science.* 268:1045–1049.
17. Cannell, M. B., and C. Soeller. 1997. Numerical analysis of ryanodine receptor activation by L-type channel activity in the cardiac muscle diad. *Biophys. J.* 73:112–122.
18. Bers, D. M., and E. Perez-Reyes. 1999. Ca channels in cardiac myocytes: Structure and function in Ca influx and intracellular Ca release. *Cardiovasc. Res.* 42:339–360.
19. Lanner, J. T., D. K. Georgiou, …, S. L. Hamilton. 2010. Ryanodine Receptors: Structure, Expression, Molecular Details, and Function in Calcium Release. *Cold Spring Harbor Perspect. Biol.* 2:a003996.
20. Takeshima, H., M. Hoshijima, and L. S. Song. 2015. Ca2+ Microdomains Organized by Junctophilins.
21. Jayasinghe, I., A. H. Clowsley, …, C. Soeller. 2018. Shining new light on the structural determinants of cardiac couplon function: Insights from ten years of nanoscale microscopy.
22. Lučić, V., F. Förster, and W. Baumeister. 2005. Structural studies by electron tomography: From cells to molecules.
23. Miranda, K., W. Girard-Dias, …, I. Ramos. 2015. Three dimensional reconstruction by electron microscopy in the life sciences: An introduction for cell and tissue biologists. *Mol. Reprod. Dev.* 82:530–547.
24. Hayashi, T., M. E. Martone, …, M. Hoshijima. 2009. Three-dimensional electron microscopy reveals new details of membrane systems for Ca2+ signaling in the heart. *J. Cell Sci.* 122:1005–1013.
25. Hake, J., A. G. Edwards, …, A. D. McCulloch. 2012. Modelling cardiac calcium sparks in a three-dimensional reconstruction of a calcium release unit. *J. Physiol. (Lond.).* 590:4403–4422.
26. Ladd, D., A. Tilūnaitė, …, V. Rajagopal. 2019. Assessing Cardiomyocyte Excitation-Contraction Coupling Site Detection From Live Cell Imaging Using a Structurally-Realistic Computational Model of Calcium Release. *Front. Physiol.* 10:1263.
27. Koivumäki, J. T., J. Hoffman, …, J. Sundnes. 2022. Computational cardiac physiology for new modelers: Origins, foundations, and future.
28. Bers, D. M. 2002. Cardiac excitation contraction coupling. *Nature.* 415:198–205.
29. Barclay, C. J. 2012. Quantifying Ca2+ release and inactivation of Ca2+ release in fast- and slow-twitch muscles. *J. Physiol.* 590:6199–6212.
30. Stiles, J. R., and T. M. Bartol. 2001. Monte Carlo Methods for Simulating Realistic Synaptic Microphysiology using MCELL. *In* Computational Neuroscience: Realistic Modeling for Experimentalists CRC Press, chapter 4.
31. Kerr, R. A., T. M. Bartol, …, J. R. Stiles. 2008. Fast Monte Carlo Simulation Methods for Biological Reaction-Diffusion Systems in Solution and on Surfaces. *SIAM J. Sci. Comput.* 30:3126–3149.
32. Czech, J., M. Dittrich, and J. R. Stiles. 2009. Rapid creation, Monte Carlo simulation, and visualization of realistic 3D cell models. *Methods Mol. Biol.* 500:237–287.
33. Husar, A., M. Ordyan, …, T. J. Sejnowski. 2022. MCell4 with BioNetGen: A Monte Carlo Simulator of Rule-Based Reaction-Diffusion Systems with Python Interface. Preprint at bioRxiv. https://doi.org/10.1101/2022.05.17.492333.
34. Koh, X., B. Srinivasan, …, A. Levchenko. 2006. A 3D Monte Carlo analysis of the role of dyadic space geometry in spark generation. *Biophys. J.* 90:1999–2014.
35. Valent, I., A. Zahradníková, …, I. Zahradník. 2007. Spatial and temporal Ca2+, Mg2+, and ATP2-dynamics in cardiac dyads during calcium release. *Biochim. Biophys. Acta Biomembr.* 1768:155–166.
36. Cheng, H., and W. J. Lederer. 2008. Calcium Sparks. *Physiol. Rev.* 88:1491–1545.
37. Mastronarde, D. N. 2008. Correction for non-perpendicularity of beam and tilt axis in tomographic reconstructions with the IMOD package. *In* Journal of Microscopy.
38. Yu, Z., M. J. Holst, and J. A. McCammon. 2008. High-fidelity geometric modeling for biomedical applications. *Finite Elem. Anal. Des.* 44:715–723.

39. Lee, C. T., J. B. Moody, …, M. J. Holst. 2019. The implementation of the colored abstract simplicial complex and its application to mesh generation. *ACM Trans. Math Software.* 45:28.

40. Das, T., and M. Hoshijima. 2013. Adding a new dimension to cardiac nano-architecture using electron microscopy: Coupling Membrane Excitation to Calcium Signaling.

41. Asghari, P., D. R. L. Scriven, …, E. D. W. Moore. 2014. Nonuniform and variable arrangements of ryanodine receptors within mammalian ventricular couplons. *Circ. Res.* 115:252–262.

42. Peng, W., H. Shen, …, N. Yan. 2016. Structural basis for the gating mechanism of the type 2 ryanodine receptor RyR2. *Science.* 354:aah5324.

43. Bers, D. M. 2001. Excitation-contraction Coupling and Cardiac Contractile Force, 237, 2nd edition. Kluwer Academic Publishers.

44. Picht, E., A. V. Zima, …, D. M. Bers. 2011. Dynamic Calcium Movement Inside Cardiac Sarcoplasmic Reticulum During Release. *Circ. Res.* 108:847–856.

45. Robertson, S. P., J. D. Johnson, and J. D. Potter. 1981. The time-course of Ca2+ exchange with calmodulin, troponin, parvalbumin, and myosin in response to transient increases in Ca2+. *Biophys. J.* 34:559–569.

46. Fabiato, A. 1983. Calcium-induced release of calcium from the cardiac sarcoplasmic reticulum. *Am. J. Physiol. Cell Physiol.* 245:C1–C14.

47. Michailova, A., F. DelPrincipe, …, E. Niggli. 2002. Spatiotemporal features of Ca2+ buffering and diffusion in atrial cardiac myocytes with inhibited sarcoplasmic reticulum. *Biophys. J.* 83:3134–3151.

48. Bondarenko, V. E. 2004. Computer model of action potential of mouse ventricular myocytes. *Am. J. Physiol. Heart Circ. Physiol.* 287:H1378–H1403.

49. Shannon, T. R., and D. M. Bers. 1997. Assessment of intra-SR free [Ca] and buffering in rat heart. *Biophys. J.* 73:1524–1531.

50. Penheiter, A. R., Z. Bajzer, …, A. J. Caride. 2003. A Model for the Activation of Plasma Membrane Calcium Pump Isoform 4b by Calmodulin. *Biochemistry.* 42:12115–12124.

51. Brini, M., and E. Carafoli. 2009. Calcium Pumps in Health and Disease. *Physiol. Rev.* 89:1341–1378.

52. Hilgemann, D. W., D. A. Nicoll, and K. D. Philipson. 1991. Charge movement during Na+translocation by native and cloned cardiac Na+/Ca2+exchanger. *Nature.* 352:715–718.

53. Higgins, E. R., M. B. Cannell, and J. Sneyd. 2006. A buffering SERCA pump in models of calcium dynamics. *Biophys. J.* 91:151–163.

54. Saftenku, E., A. J. Williams, and R. Sitsapesan. 2001. Markovian models of low and high activity levels of cardiac ryanodine receptors. *Biophys. J.* 80:2727–2741.

55. Greenstein, J. L., and R. L. Winslow. 2002. An integrative model of the cardiac ventricular myocyte incorporating local control of Ca2+ release. *Biophys. J.* 83:2918–2945.

56. Wang, J., E. Gao, …, J. Y. Cheung. 2013. Induced overexpression of Na+/Ca2+ exchanger does not aggravate myocardial dysfunction induced by transverse aortic constriction. *J. Card. Fail.* 19:60–70.

57. Amin, A. S., H. L. Tan, and A. A. Wilde. 2010. Cardiac ion channels in health and disease. *Heart Rhythm.* 7:1870–1871.

58. Lipskaia, L., Z. Keuylian, …, R. Bobe. 2014. Expression of sarco (endo) plasmic reticulum calcium ATPase (SERCA) system in normal mouse cardiovascular tissues, heart failure and atherosclerosis. *Biochim. Biophys. Acta.* 1843:2705–2718.

59. Franzini-Armstrong, C., and D. G. Ferguson. 1985. Density and disposition of Ca2+-ATPase in sarcoplasmic reticulum membrane as determined by shadowing techniques. *Biophys. J.* 48:607–615.

60. Guo, T., D. Gillespie, and M. Fill. 2012. Ryanodine Receptor Current Amplitude Controls Ca2+ Sparks in Cardiac Muscle. *Circ. Res.* 111:28–36.

61. Fill, M., and J. A. Copello. 2002. Ryanodine receptor calcium release channels. *Physiol. Rev.* 82:893–922.

62. Song, D. W., J. G. Lee, …, D. H. Kim. 2011. Ryanodine receptor assembly: a novel systems biology approach to 3D mapping. *Prog. Biophys. Mol. Biol.* 105:145–161.

63. Cannell, M. B., C. H. T. Kong, …, D. R. Laver. 2013. Control of sarcoplasmic reticulum Ca2+ release by stochastic RyR gating within a 3D model of the cardiac dyad and importance of induction decay for CICR termination. *Biophys. J.* 104:2149–2159.

64. Milani-Nejad, N., and P. M. Janssen. 2014. Small and large animal models in cardiac contraction research: Advantages and disadvantages. *Pharmacol. Ther.* 141:235–249.

65. Louch, W. E., J. E. Hake, …, O. M. Sejersted. 2010. Control of Ca2+release by action potential configuration in normal and failing murine cardiomyocytes. *Biophys. J.* 99:1377–1386.

66. Vitale, G., R. Coppini, …, C. Ferrantini. 2021. T-tubule remodeling in human hypertrophic cardiomyopathy. *J. Muscle Res. Cell Motil.* 42:305–322.

67. Song, L. S., E. A. Sobie, …, H. Cheng. 2006. Orphaned ryanodine receptors in the failing heart. *Proc. Natl. Acad. Sci. USA.* 103:4305–4310.

68. Louch, W. E., J. T. Koivumäki, and P. Tavi. 2015. Calcium signalling in developing cardiomyocytes: Implications for model systems and disease. *J. Physiol.* 593:1047–1063.

69. Cannell, M. B., D. J. Crossman, and C. Soeller. 2006. Effect of changes in action potential spike configuration, junctional sarcoplasmic reticulum micro-architecture and altered t-tubule structure in human heart failure. *J. Muscle Res. Cell Motil.* 27:297–306.

70. Autin, L., M. Maritan, …, D. S. Goodsell. 2020. Mesoscope: AWeb-based Tool for Mesoscale Data Integration and Curation. *In* MolVA 2020 - Workshop on Molecular Graphics and Visual Analysis of Molecular Data.

71. Berman, H., K. Henrick, and H. Nakamura. 2003. Announcing the worldwide Protein Data Bank. *Nat. Struct. Biol.* 10:980.

72. Klein, T., L. Autin, …, I. Viola. 2018. Instant Construction and Visualization of Crowded Biological Environments. *IEEE Trans. Visual. Comput. Graph.* 24:862–872.

73. Sehnal, D., S. Bittrich, …, A. S. Rose. 2021. Mol*Viewer: Modern web app for 3D visualization and analysis of large biomolecular structures. *Nucleic Acids Res.* 49:W431–W437.

74. Wehrens, X. H., S. E. Lehnart, and A. R. Marks. 2005. Intracellular calcium release and cardiac disease. *Annu. Rev. Physiol.* 67:69–98.

75. Brochet, D. X. P., D. Yang, …, W. J. Lederer. 2012. Elementary calcium release events from the sarcoplasmic reticulum in the heart. *Adv. Exp. Med. Biol.* 740:499–509.

76. Eisner, D. A., J. L. Caldwell, …, A. W. Trafford. 2017. Calcium and Excitation-Contraction Coupling in the Heart. *Circ. Res.* 121:181–195.

77. Poláková, E., and E. A. Sobie. 2013. Alterations in T-tubule and dyad structure in heart disease: Challenges and opportunities for computational analyses.

78. Shiferaw, Y., G. L. Aistrup, …, J. A. Wasserstrom. 2020. Remodeling Promotes Proarrhythmic Disruption of Calcium Homeostasis in Failing Atrial Myocytes. *Biophys. J.* 118:476–491.

79. Quarteroni, A., T. Lassila, …, R. Ruiz-Baier. 2017. Integrated Heart—Coupling multiscale and multiphysics models for the simulation of the cardiac function. *Comput. Methods Appl. Mech. Eng.* 314:345–407.

80. Williams, G. S. B., G. D. Smith, …, M. S. Jafri. 2010. Models of cardiac excitation-contraction coupling in ventricular myocytes. *Math. Biosci.* 226:1–15.

81. Shkryl, V. M., L. A. Blatter, and E. Ríos. 2012. Properties of Ca 2+ sparks revealed by four-dimensional confocal imaging of cardiac muscle. *J. Gen. Physiol.* 139:189–207.

82. Walker, M. A., G. S. B. Williams, …, R. L. Winslow. 2014. Superresolution Modeling of Calcium Release in the Heart. *Biophys. J.* 107:3018–3029.

83. Clancy, C. E., and R. S. Kass. 2002. Defective cardiac ion channels: From mutations to clinical syndromes. *J. Clin. Invest.* 110:1075–1077.
84. Hirakis, S. P. 2019. Multiscale Analysis and Visualization of Biophysical Structure and Biochemical Function with Computational Microscopy, Ph.D. thesis.
85. Berridge, M. J., M. D. Bootman, and H. L. Roderick. 2003. Calcium signalling: Dynamics, homeostasis and remodelling. *Nat. Rev. Mol. Cell Biol.* 4:517–529.
86. Bers, D. M. 2010. CaMKII inhibition in heart failure makes jump to human. *Circ. Res.* 107:1044–1046.
87. Kim, J. C., M. J. Son, …, S. H. Woo. 2010. IP3-induced cytosolic and nuclear Ca2+ signals in HL-1 atrial myocytes: possible role of IP3 receptor subtypes. *Mol. Cell.* 29:387–395.
88. Jones, D. C., and E. A. Sobie. 2023. Modeling the spatiotemporal properties of crosstalk between RYR and IP3R-mediated Ca2+release in failing cardiomyocytes. *Biophys. J.* 122:165a.
89. Boras, B. W., A. Kornev, …, A. D. McCulloch. 2014. Using Markov state models to develop a mechanistic understanding of protein kinase A regulatory subunit RIalpha activation in response to cAMP binding. *J. Biol. Chem.* 289:30040–30051.
90. Agarwal, S. R., J. Gratwohl, …, R. D. Harvey. 2018. Membrane Domains and cAMP Compartmentation in Cardiac Myocytes. *Biophys. J.* 114:502a.
91. Yang, P. C., B. W. Boras, …, C. E. Clancy. 2016. A Computational Modeling and Simulation Approach to Investigate Mechanisms of Subcellular cAMP Compartmentation. *PLoS Comput. Biol.* 12:e1005005.
92. Morotti, S., A. G. Edwards, …, E. Grandi. 2014. A novel computational model of mouse myocyte electrophysiology to assess the synergy between Na+loading and CaMKII. *J. Physiol.* 592:1181–1197.
93. Song, Z., L. H. Xie, …, Z. Qu. 2019. A Spatiotemporal Ventricular Myocyte Model Incorporating Mitochondrial Calcium Cycling. *Biophys. J.* 117:2349–2360.
94. Garcia, G. C., T. M. Bartol, …, A. Skupin. 2019. Mitochondrial morphology provides a mechanism for energy buffering at synapses. *Sci. Rep.* 9:18306.
95. Ingólfsson, H. I., C. Arnarez, …, S. J. Marrink. 2016. Computational 'microscopy' of cellular membranes.
96. Shen, X., J. v. den Brink, …, W. E. Louch. 2018. 3D dSTORM Imaging Reveals Disassembly of Ryanodine Receptor Clusters in Failing Cardiomyocytes. *Biophys. J.* 114:621a.
97. Asghari, P., D. R. Scriven, …, E. D. Moore. 2020. Cardiac ryanodine receptor distribution is dynamic and changed by auxiliary proteins and post-translational modification. *Elife.* 9:e51602.
98. Shen, X., T. R. Kolstad, …, W. E. Louch. 2020. 3D Dstorm Imaging Reveals Camkii-Dependent Dispersal of Ryanodine Receptor Clusters in Failing Rat Cardiomyocytes. *Biophys. J.* 118:529a–530a.
99. Mesa, M. H., J. v. den Brink, …, P. Rangamani. 2022. Nanoscale organization of ryanodine receptor distribution and phosphorylation pattern determines the dynamics of calcium sparks. *Biophys. J.* 121:378a.
100. Kolstad, T. R., J. van den Brink, …, W. E. Louch. 2018. Ryanodine receptor dispersion disrupts Ca2+ release in failing cardiac myocytes. *eLife.* 7:e39427.
101. Asghari, P., D. R. Scriven, …, E. D. Moore. 2022. RYR2 phosphomutants show that the tetramers and the junctional sarcoplasmic reticulum form a structural syncytium. *J. Gen. Physiol.* 154
102. Huber, G. A., and J. A. McCammon. 2010. Browndye: A software package for Brownian dynamics. *Comput. Phys. Commun.* 181:1896–1905.
103. Aswath, A., A. Alsahaf, …, G. Azzopardi. 2023. Segmentation in large-scale cellular electron microscopy with deep learning: A literature survey. *Med. Image Anal.* 89:102920.
104. Marchena, M., B. Echebarria, …, E. Alvarez-Lacalle. 2020. Buffering and total calcium levels determine the presence of oscillatory regimes in cardiac cells. *PLoS Comput. Biol.* 16:e1007728.
105. Navarro, P. P. 2022. Quantitative Cryo-Electron Tomography. *Front. Mol. Biosci.* 9:934465.
106. Young, L. N., and E. Villa. 2023. Bringing Structure to Cell Biology with Cryo-Electron Tomography. *Annu. Rev. Biophys.* 52:573–595.
107. Stevens, J. A., F. Grünewald, …, S. J. Marrink. 2023. Molecular dynamics simulation of an entire cell. *Front. Chem.* 11:1106495.